Geol. Mag. **149** (3), 2012, pp. 483–506. © Cambridge University Press 2011
doi:10.1017/S0016756811000811

The Liuyuan complex in the Beishan, NW China: a Carboniferous–Permian ophiolitic fore-arc sliver in the southern Altaids

QIGUI MAO*‡, WENJIAO XIAO‡†, BRIAN F. WINDLEY§, CHUNMING HAN‡, JUNFENG QU‡, SONGJIAN AO‡, JI'EN ZHANG‡ & QIANQIAN GUO‡

*Beijing Institute of Geology for Mineral Resources, Beijing 100012, China
‡State Key Laboratory of Lithospheric Evolution, Institute of Geology and Geophysics, Chinese Academy of Sciences, Beijing 100029, China
§Department of Geology, University of Leicester, Leicester LE1 7RH, UK

(*Received* 27 October 2010; *accepted* 21 March 2011; *first published online* 6 October 2011)

Abstract – The tectonic history and time of closure of the Palaeo-Asian ocean of the Altaids are issues of lively current debate. To address these issues, this paper presents detailed geological, petrological and geochemical data of the Liuyuan complex (LC) in the Beishan region in NW China, located in the southernmost Altaids, in order to constrain its age, origin and tectonic setting. The LC mainly comprises massive basalts, pillow basalts, basaltic breccias, gabbros and ultramafic rocks together with cherts and tuffs. Most prominent are gabbros and large volumes of basaltic lavas. These mafic rocks have high TiO_2 contents, flat rare earth element (REE) patterns and show high-field-strength elements (HFSEs) similar to those of mid-ocean ridge basalts (MORB). The mafic rocks exhibit positive $\varepsilon_{Nd(t)}$ (6.6–9.0) values, representing magmas derived from the mantle. But these basic rocks are also enriched in Th relative to REEs, and are systematically depleted in Nb–Ta–(Ti) relative to REEs. There is also a large range in initial $^{87}Sr/^{86}Sr$ (0.7037–0.7093). All these variables indicate that mantle-derived magma was contaminated by fluids and/or melts from a subducting lithospheric slab, and formed in a supra-subduction zone (SSZ) setting. A gabbro intruded in the complex was dated by LA-ICP-MS on 20 zircons that yielded a $^{206}Pb–^{238}U$ weighted average age of 286 ± 2 Ma. Considering the fact that all these basalts are imbricated against Permian tuffaceous sediments and limestone, we propose that the LC formed as an ophiolite in a fore-arc in Carboniferous–Permian time. This indicates that the Palaeo-Asian ocean still existed at 286 ± 2 Ma in early Permian time, and thus the time of closure of the Palaeo-Asian ocean was in or after the late Permian.

Keywords: Carboniferous–Permian, Liuyuan complex, accretionary orogenesis, Beishan, southern Altaids.

1. Introduction

The Altaids, located between the Siberian, North China, Tarim and East European cratons, represent one of the most important sites of juvenile crustal growth in the world (Şengör, Natal'in & Burtman, 1993; Şengör & Natal'in, 1996) (Fig. 1). After decades of study, it is widely accepted that the Altaids formed by successive accretions of island arcs, accretionary prisms, minor ophiolitic fragments and small continental blocks (Coleman, 1989; Şengör, Natal'in & Burtman, 1993; Dobretsov, Berzin & Buslov, 1995; Şengör & Natal'in, 1996; Gao *et al*. 1998; Buchan *et al*. 2002; Bazhenov *et al*. 2003; Xiao *et al*. 2003, 2004*a,b*, 2008; Windley *et al*. 2007). The closure of the Palaeo-Asian ocean terminated the accretionary history of the Altaids. However, the timing of the final suture has been hotly debated (Coleman, 1989; Zuo *et al*. 1990, 1991; Shi *et al*. 1994; Han *et al*. 1997; Ma, Shu & Sun, 1997; Gao *et al*. 1998; Xiao *et al*. 2004*b*, 2008; Zhou *et al*. 2004; Mao *et al*. 2006, 2008; Windley *et al*. 2007; Zhang *et al*. 2007).

†Author for correspondence: wj-xiao@mail.igcas.ac.cn

The Beishan mountain range in NW China, located on the southern margin of the Altaids, is a key area for unravelling the evolution and accretionary processes of the southern Altaids, and the closure time of the Palaeo-Asian ocean (Fig. 1). In particular, a Permian magmatic belt, the Liuyuan complex (LC), contains important information about the final stages of tectonic evolution of the ocean (Zuo *et al*. 1990; Zhao *et al*. 2006; Jiang *et al*. 2007). Previous studies proposed diverse models to explain the geological evolution of the Beishan and adjacent areas based on different interpretations of the LC (Zuo *et al*. 1990, 1991; Liu & Wang, 1995; Ma, Shu & Sun, 1997; Nie *et al*. 2002*a*; Xiao *et al*. 2004*b*), but no consensus emerged. For example, a Permian continental rift was favoured by those who considered that the final closure of the Palaeo-Asian ocean was before the Carboniferous (GSBGMR, 1989; Zuo *et al*. 1990; XBGMR, 1993; Liu & Wang, 1995; Ma, Shu & Sun, 1997; Zuo, Liu & Liu, 2003; Zhao *et al*. 2006; Jiang *et al*. 2007). In contrast, others argued that the Palaeo-Asian ocean did not close until late Permian time or later (Shi *et al*. 1994; Zhu, 1997; Xiao *et al*. 2003, 2004*b*, 2008; Windley *et al*. 2007).

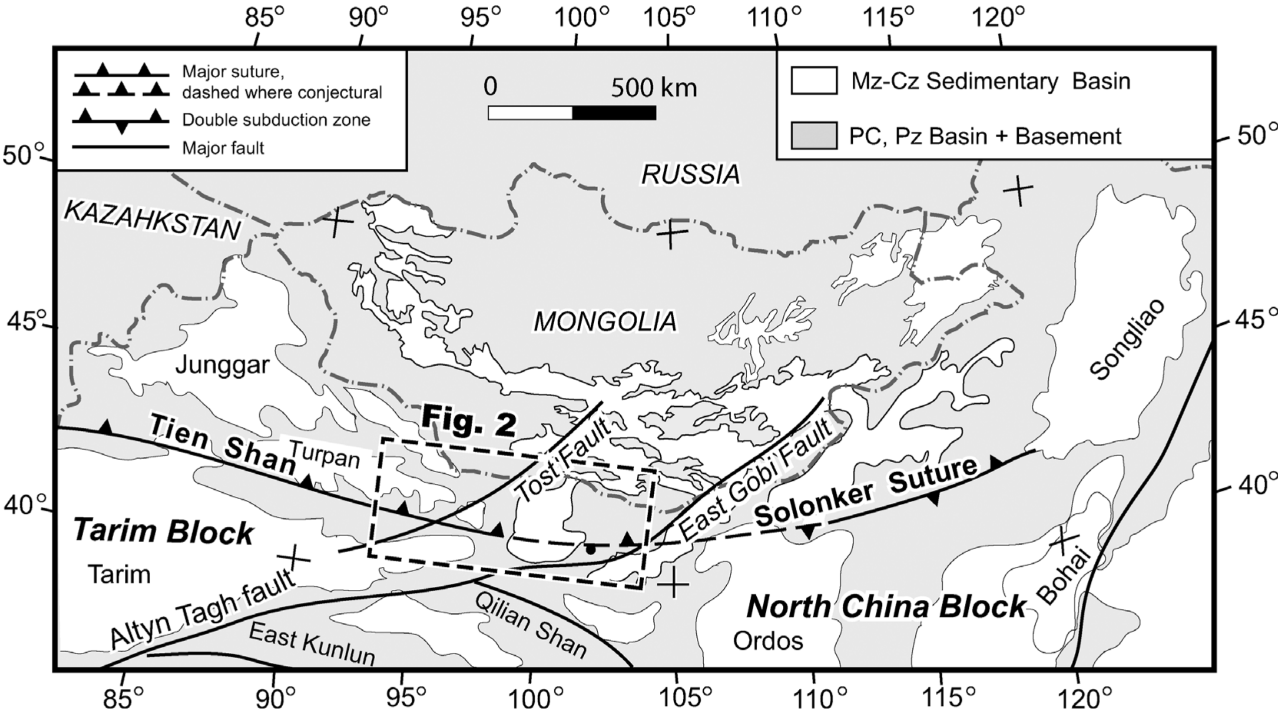

Figure 1. Simplified tectonic map of the southern and eastern Altaids showing the tectonic position of the Beishan orogen (based on our observations and modified after Liu & Wang (1995), Hendrix *et al.* (1996), Hendrix (2000), Lamb & Badarch (2000) and Lamb *et al.* (2008). PC – Precambrian; Pz – Palaeozoic; Mz – Mesozoic; Cz – Cenozoic. Location of Figure 2 is marked.

In this paper, we use detailed mapping, structural data, major–trace element and isotope geochemistry, and isotopic ages to place tight constraints on the petrogenesis and tectonic setting of the LC, and accordingly to establish the terminal processes on the southernmost margin of the Altaids.

2. Geological setting

The Beishan mountain range is composed of several arc belts that are separated by six ophiolite-bearing melange zones, which are marked today as major faults, shown in Figures 1 and 2a (Zuo *et al.* 1990, 1991; Liu & Wang 1995; Nie *et al.* 2002*a*). Xiao *et al.* (2010*b*) made detailed descriptions of the regional geology; here we introduce just the geology associated with the LC.

In the study area, four tectonic units are recognized: the Shuangyingshan arc, the Huaniushan arc, the Liuyuan complex and the Shibanshan arc (Fig. 2a, b). The Shuangyingshan arc consists of Precambrian to Ordovician shelf carbonates and clastic sediments including limestones, flysch, black cherts and highly metamorphosed clastic sediments that are now mainly migmatitic paragneisses, schists and marbles. Cambrian sediments are characterized by black shales and interbedded carbonates.

The Huaniushan arc, developed on the Shuangyingshan arc, comprises Ordovician–Permian calc-alkaline basalts, andesites, rhyolites, tuffs and volcaniclastic rocks with interlayered clastic sediments and carbonates (Zuo *et al.* 1990; Liu & Wang 1995; Nie *et al.* 2002*a*). Along the southern margin of the arc there are discontinuous belts of gneisses, migmatites, schists and marbles that have greenschist to eclogite-facies mineral assemblages (Mei *et al.* 1998, 1999; Yang *et al.* 2006). Eclogites at Gubaoquan (Fig. 2a) were designated an early Ordovician–Silurian age mainly by regional correlations; this was confirmed by a zircon age of 465 ± 10 Ma (GSBGMR 1989; Yu *et al.* 1999; Yang *et al.* 2006; Liu *et al.* 2011; Qu *et al.* 2011). The ages of granitoids in the Shuangyingshan–Huaniushan multiple arc range from Silurian to early Triassic (GSBGMR, 1989; Tian, 1993; Nie *et al.* 2002*a*,*b*; Zhao, Guo & Wang, 2007). For example, Zhao, Guo & Wang (2007) reported sensitive high-resolution ion microprobe (SHRIMP) zircon U–Pb ages of 423 ± 8 Ma, 397 ± 7 Ma and 436 ± 9 Ma for granodiorites, monzogranites and potassium granites, respectively. An adakite has a zircon U–Pb age of 424 ± 4 Ma (Mao *et al.* 2010), the Shijingpo granite has a zircon U–Pb age of 380 ± 12 Ma (Tian, 1993) and the Huaniushan and Huitongshan alkaline granites have ^{40}Ar–^{39}Ar ages on potassium feldspar of 192 ± 2 Ma and 194 ± 1 Ma, respectively (Nie *et al.* 2002*b*; Jiang *et al.* 2003).

The late Palaeozoic Shibanshan arc, located on the northern margin of the Dunhuang block (Fig. 2a, b), contains a low-grade and a high-grade metamorphic unit. The low-grade unit, on the northern margin of the arc, contains low greenschist-facies Devonian–Permian calc-alkaline volcanic rocks, volcaniclastic rocks, tuffs, carbonates and clastic rocks. The high-grade unit is mainly composed of gneisses, migmatites, schists, mylonitic schists and marbles. Previously published ages for these metamorphic rocks were mainly designated by comparison with similar rocks nearby; several contrasting ages such as Proterozoic, Ordovician–

https://doi.org/10.1017/S0016756811000811 Published online by Cambridge University Press

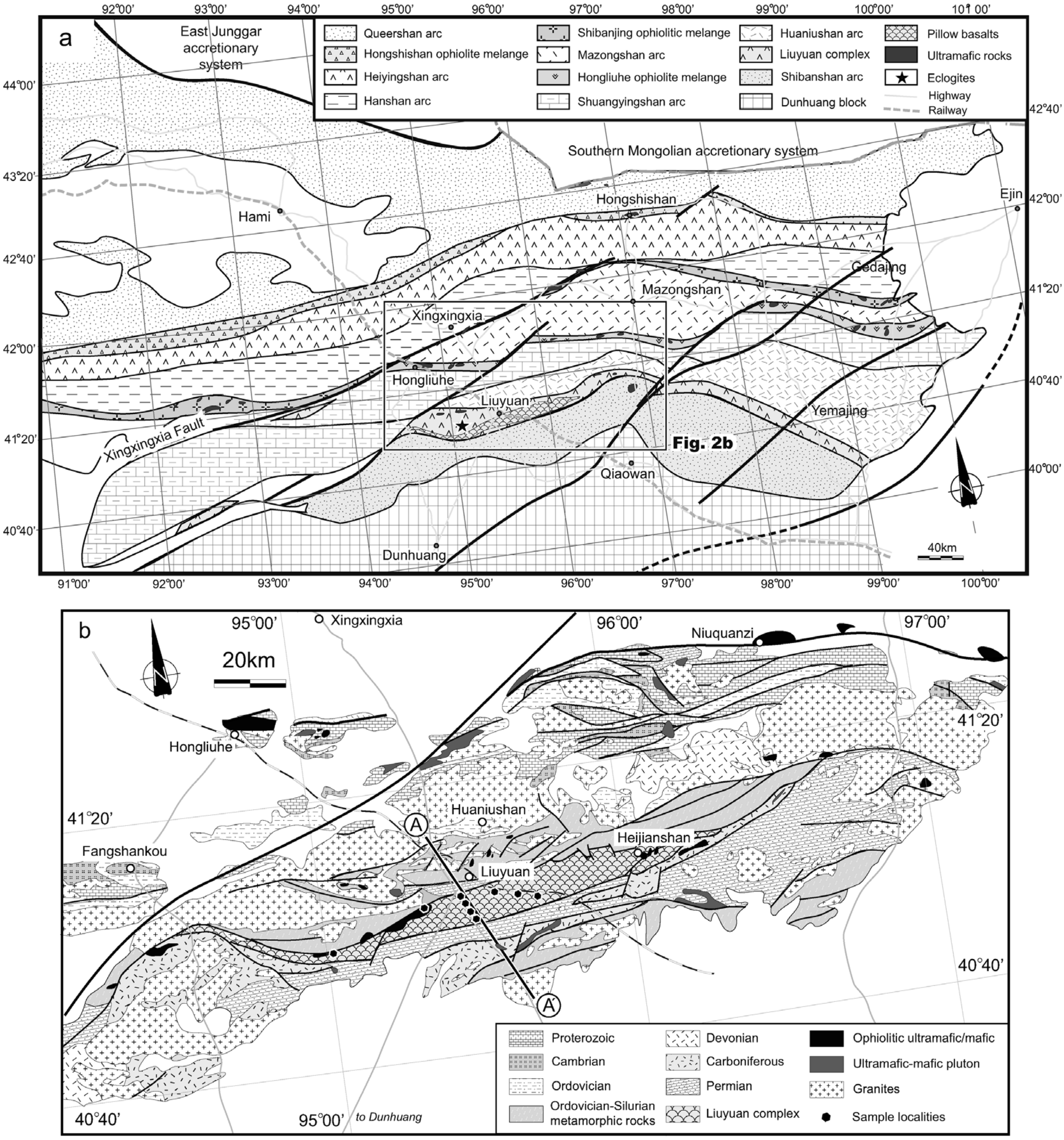

Figure 2. (a) Tectonic map of the southern part of the Beishan orogen, showing the position of the Liuyuan complex in relation to the three main arcs (based on our observations and modified after Liu & Wang, 1995; Nie *et al*. 2002*a*). (b) A geological map of the Liuyuan and adjacent areas showing the relationships between the main stratigraphic units of the Beishan (modified after GSBGMR, 1989; Zuo *et al*. 1990; Nie *et al*. 2002*a*). Black dots mark sample locations.

Silurian or Permian were suggested (GSBGMR, 1989; Liu & Wang 1995; Yu *et al*. 1999; Yang *et al*. 2006). The metamorphic rocks have a whole-rock Rb–Sr age of 548 Ma (Zuo *et al*. 1990). Both units contain abundant Carboniferous–early Triassic granitic intrusions (Zuo *et al*. 1990; Nie *et al*. 2002*a*).

The Liuyuan complex, located between the Huaniushan arc and the Shibanshan arc (Fig. 2a, b), contains greenschist-grade ophiolitic rocks (cherts, basalts, gabbros, ultramafic rocks) and intrusive batholiths and small plutons of diorite, granodiorite, biotite granite and alkali-granite (Zuo *et al*. 1990; Liu & Wang, 1995; Nie *et al*. 2002*a*; Zhao, Guo & Wang, 2007).

3. Field relations and petrology of the Liuyuan ophiolitic complex

3.a. Field relations

The ENE–WSW-trending Liuyuan complex, located between the Huaniushan arc and the Shibanshan arc, is up to 20 km wide (Fig. 2b), and contains

https://doi.org/10.1017/S0016756811000811 Published online by Cambridge University Press

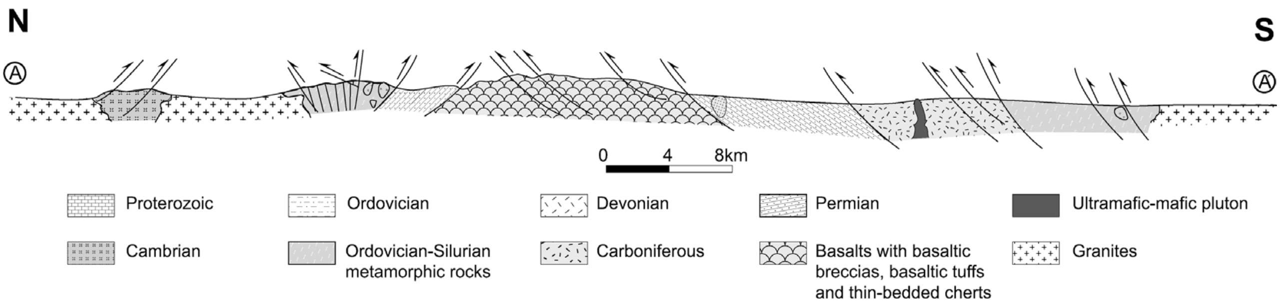

Figure 3. Cross-section of the Liuyuan complex along the line A–A′ marked in Figure 2b, based on our field observations and mapping, and modified after GSBGMR (1989).

many imbricated thrust sheets. Samples for this study were mainly collected along two profiles illustrated in Figure 2b, plus some from the Heijianshan area (Fig. 2b). The complex comprises ultramafic rocks, gabbros, massive basalts, abundant pillow basalts, hyaloclastic pillow breccias, volcaniclastic breccias, basaltic tuffs and thin-bedded cherts. In several parts of the stratigraphy, volcaniclastic breccias up to 16 m thick consist of rhyolitic fragments in an andesitic matrix. The ultramafic rocks and some gabbros are located along faults on the northern margin of the complex (Fig. 2b). A characteristic of the complex is the abundance of hydrothermal veins that are predominantly filled by epidote with minor quartz, haematite and Fe carbonate.

Along the National Highway (Fig. 2b) all lithologies (except for ultramafic rocks) of the complex are well preserved and displayed. The best-preserved, structurally-intact sections show that the original stratigraphic succession was from bottom to top: olivine gabbro/massive gabbro (Fig. 4f), massive basalt, pillow basalt, basaltic volcaniclastic tuff and breccia, deep-sea chert with beds of tuff (Fig. 4a–c, e), and late hornblende gabbro (Fig. 4d). Thrusts have affected the whole complex, and have preferentially developed along beds of tuff and chert; as a result the whole complex is an imbricated thrust stack up to 20 km wide, with thrust directions towards the NNW (Fig. 3). In the main volcanic pile, fine-grained gabbroic dykes and late hornblende gabbro dykes (Fig. 4d) have intruded the basaltic rocks. Many olivine gabbros (Fig. 4f) crop out along the northern margin of the complex.

In the more intensively deformed Heijianshan (Fig. 2b) area, greenschist-facies metamorphosed gabbros and mafic volcanic rocks with elongate pillows (Fig. 4b) have been thrust to the SE. Several lenses of serpentinized ultramafic rocks occur along the faults (Fig. 4g).

3.b. Petrology of the Liuyuan complex

The ultramafic rocks include peridotites with variable degrees of serpentinization. Olivine is only preserved as inclusions in clinopyroxene, but some fine-grained spinels have survived the serpentinization. The ultramafic rocks are an important component of the LC, but we will focus on the mafic rocks in the later sections on geochemistry and geochronology, because ultramafic rocks are difficult to date and cannot be treated as magmas.

There are three types of slightly altered gabbro. The first, exposed in the northern margin of the LC, is olivine gabbro that consists of olivine, orthopyroxene, clinopyroxene, plagioclase and minor opaques. Subhedral–anhedral orthopyroxenes and clinopyroxenes are situated between euhedral plagioclases. Plagioclase contains a few inclusions of clinopyroxene. The second type is massive gabbro, exposed at the base of the basalts, made up of euhedral plagioclase, euhedral–subhedral clinopyroxene, magnetite, ilmenite, a little olivine and minor accessories; ilmenite content locally reaches 2–3 %. Plagioclase is replaced by clay minerals and sericite in many samples. The third type is hornblende gabbro that forms dykes (DQ43) (which traverse all rocks of the complex) composed of clinopyroxene, plagioclase, hornblende and minor opaques. The margins of clinopyroxenes are partly replaced by hornblende, and plagioclase is partly replaced by clay minerals and sericite.

Most basalts are slightly altered, except for those in the Heijianshan area. Most basalts are cut by a few carbonate veins, and a few contain amygdales. Basaltic rocks are composed of plagioclase, magnetite, ilmenite, minor olivine and volcanic glass, and some samples have a little clinopyroxene. A few samples are enriched in ilmenite up to 2–3 %. Jiang *et al.* (2007) reported that basalts mainly consist of albite ($Ab_{100–91}$) and clinopyroxene ($En_{45–46}$). To avoid any possible effects of alteration, we chose the freshest rocks for our geochemical study.

4. Geochemistry

Representative major and trace element analyses are listed in Table 1. Details of analytical methodology are given in Appendix 1. The different types of mafic rocks (gabbros and basalts) have similar major element compositions, except for TiO_2 (Table 1; Figs 5, 6). The mafic rocks are characterized by a range of SiO_2 (46.0–52.1 wt %), TiO_2 (1.2–3.6 wt %), Al_2O_3 (11.6–16.1 wt %), MgO (4.1–7.9 wt %), TFe_2O_3 (8.5–14.9 wt %), CaO (6.1–11.4 wt %), MnO (0.14–0.27 wt %) and

https://doi.org/10.1017/S0016756811000811 Published online by Cambridge University Press

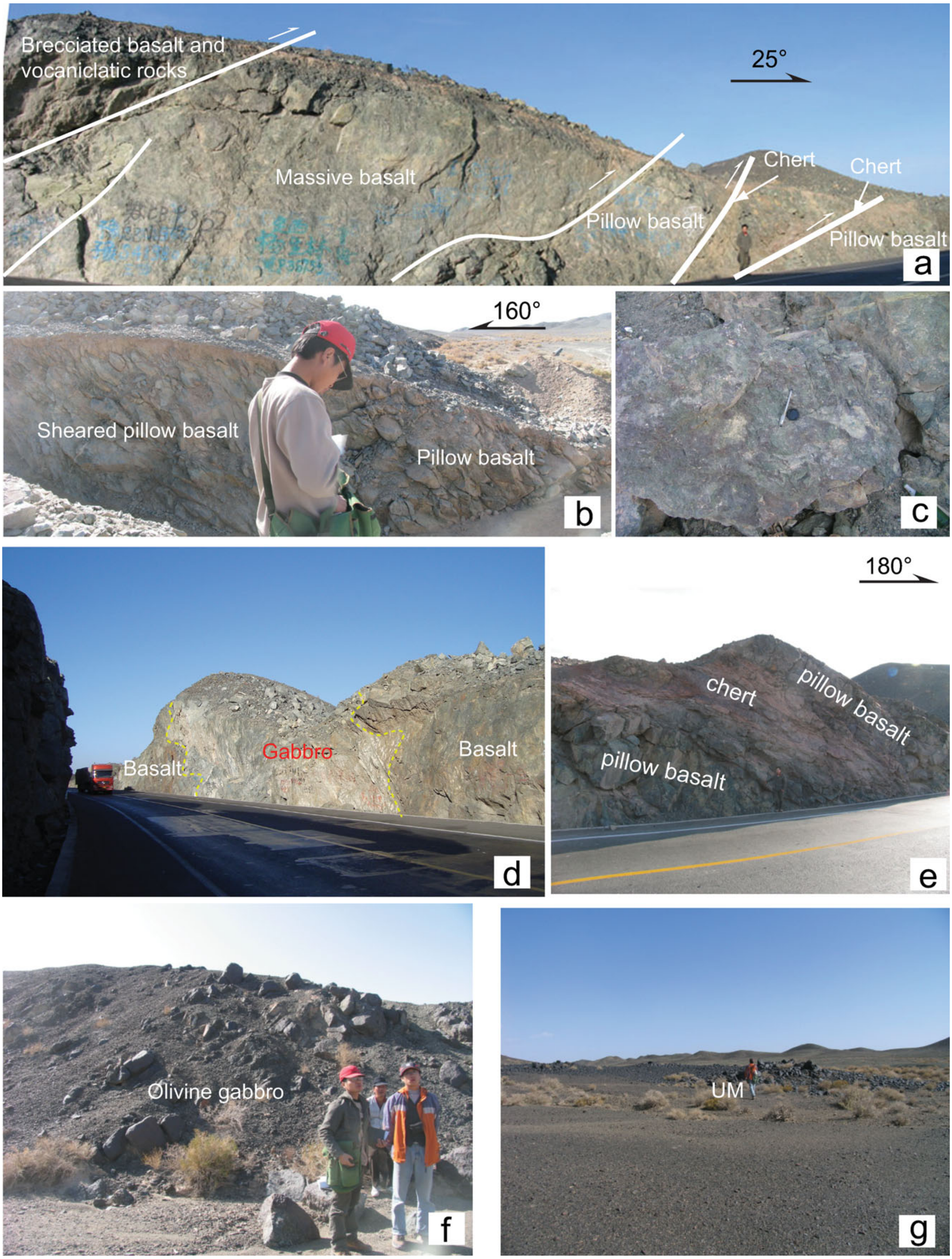

Figure 4. (Colour online) Field photos of the Liuyuan complex, Beishan. (a) Massive and pillow basalts imbricated by out-of-sequence thrusts with beds of chert and brecciated basalt, Liuyuan; (b) sheared pillow basalts, Heijianshan; (c) basaltic breccia, Liuyuan; (d) a gabbro dyke intruded into basalt. This is the locality where DQ-43 was sampled for geochronology, Liuyuan; (e) thin-bedded cherts between pillow basalts; (f) olivine gabbro on the northern margin of the Liuyuan complex; (g) ultramafic rocks in the Heijianshan area.

https://doi.org/10.1017/S0016756811000811 Published online by Cambridge University Press

Table 1. The major (wt %) and trace element (ppm) analyses of the Liuyuan complex, NW China

	Olivine gabbros				Massive gabbros		Hornblende gabbros			Group 1 basalts						
samples	LYB17-4	LYB18-1	LYB18-4	LYB18-6	9LY04-1	9LY04-3	DQ43-1	DQ43-2	DQ43-8	9LY03-2	9LY03-6	DQ42-6	DQ42-9	DQ53-1	DQ53-3	DQ56
SiO_2	48.59	46.05	47.18	47.42	47.39	47.39	50.27	49.98	50.15	47.53	48.64	48.95	48.98	50.88	51.03	47.92
TiO_2	1.99	2.49	1.75	1.85	2.02	2.03	1.19	1.40	1.34	1.64	1.63	1.57	1.60	1.79	1.73	1.70
Al_2O_3	14.43	14.31	14.07	14.33	14.95	14.91	14.83	16.46	16.09	14.89	15.31	14.12	14.42	13.92	14.44	12.63
TFe_2O_3	11.97	13.92	11.32	12.22	11.73	11.88	9.30	8.80	8.54	11.54	10.30	11.65	11.70	11.4	10.74	13.83
MnO	0.18	0.24	0.22	0.23	0.18	0.16	0.15	0.14	0.14	0.18	0.16	0.16	0.18	0.17	0.14	0.27
MgO	6.58	5.95	6.44	7.09	7.61	7.40	7.86	6.87	6.59	6.87	5.57	7.55	7.51	7.43	6.07	5.63
CaO	7.19	6.08	8.38	7.64	8.46	8.09	11.40	10.16	10.77	10.38	10.96	8.99	8.94	6.90	7.76	6.75
Na_2O	4.10	4.37	3.60	3.36	4.05	4.23	2.74	3.17	3.30	3.51	3.98	3.00	3.03	5.07	5.25	5.06
K_2O	0.95	0.32	0.70	0.73	0.47	0.33	0.47	0.48	0.57	0.30	0.40	1.17	1.04	0.08	0.32	0.17
P_2O_5	0.22	0.26	0.16	0.17	0.26	0.25	0.13	0.17	0.17	0.16	0.16	0.15	0.15	0.15	0.14	0.15
LOI	3.68	6.35	6.14	5.01	2.87	3.2	1.33	1.89	1.85	2.56	2.60	2.38	2.00	2.02	1.95	6.25
Total	99.88	100.34	99.95	100.05	99.99	99.87	99.67	99.51	99.51	99.57	99.71	99.68	99.55	99.81	99.57	100.35
Mg no.	52	46	53	53	56	55	63	61	60	54	52	56	56	56	53	45
La	8.85	9.01	6.17	6.07	4.12	4.18	7.23	7.79	7.44	4.94	4.85	4.14	4.26	4.85	4.82	4.30
Ce	24.46	26.26	17.78	17.80	11.18	11.26	19.07	21.21	19.31	14.70	14.32	12.33	13.09	14.72	14.38	13.28
Pr	3.64	4.09	2.76	2.78	1.76	1.78	2.88	3.13	2.96	2.48	2.36	2.11	2.20	2.36	2.32	2.23
Nd	17.37	20.46	13.89	13.98	8.55	8.66	13.85	14.65	14.4	12.75	11.87	11.19	11.28	12.36	12.18	11.74
Sm	5.15	6.06	4.27	4.31	2.61	2.66	4.29	4.39	4.35	3.92	3.82	3.55	3.71	3.88	3.74	3.79
Eu	1.72	1.89	1.42	1.49	0.80	0.81	1.29	1.31	1.31	1.33	1.30	1.21	1.28	1.37	1.34	1.20
Gd	6.31	7.63	5.29	5.32	2.85	2.91	4.96	5.33	5.01	4.81	4.63	4.49	4.47	4.65	4.46	4.63
Tb	1.13	1.34	0.94	0.97	0.52	0.53	0.91	0.99	0.94	0.89	0.88	0.86	0.85	0.85	0.81	0.84
Dy	7.44	8.64	6.17	6.41	3.40	3.46	6.14	6.38	6.37	5.90	5.71	5.66	5.77	5.74	5.44	5.45
Ho	1.63	1.87	1.31	1.40	0.74	0.76	1.35	1.39	1.38	1.28	1.23	1.24	1.23	1.23	1.19	1.19
Er	4.41	5.15	3.60	3.72	1.98	2.02	3.89	3.95	3.91	3.47	3.47	3.45	3.36	3.36	3.27	3.37
Tm	0.67	0.76	0.54	0.54	0.29	0.29	0.58	0.58	0.58	0.52	0.51	0.53	0.50	0.50	0.48	0.49
Yb	4.32	4.85	3.49	3.53	1.83	1.84	3.73	3.79	3.70	3.34	3.28	3.18	3.05	3.15	3.02	3.27
Lu	0.62	0.73	0.51	0.53	0.27	0.27	0.56	0.58	0.56	0.51	0.51	0.47	0.47	0.46	0.45	0.48
Sc	38.65	39.19	40.75	39.36	17.73	17.88	36.85	33.45	39.20	41.78	40.82	41.71	42.00	48.07	46.64	41.91
V	293.82	333.05	280.5	293.56	129.27	131.70	214.06	213.06	190.61	264.15	260.24	268.97	275.73	267.43	271.47	277.18
Cr	207.82	180.62	240.48	248.07	120.52	128.71	165.95	162.27	160.23	234.26	243.75	129.48	118.52	214.61	209.61	74.78
Co	37.33	40.59	39.65	41.28	19.34	19.71	32.40	34.28	31.27	45.39	42.68	41.80	45.40	47.57	43.15	37.72
Ni	61.29	48.37	64.52	63.17	48.35	47.97	50.41	57.35	48.65	70.60	68.82	51.08	46.89	61.48	45.26	24.63
Ga	18.61	20.46	16.88	17.73	8.74	8.95	17.38	18.16	16.73	16.76	15.45	16.2	17.51	13.96	14.58	15.62
Cs	2.34	1.73	3.39	3.08	0.28	0.25	0.24	0.40	0.25	1.18	0.72	0.44	0.49	0.35	0.43	2.35
Rb	42.05	12.57	28.75	31.23	4.60	7.14	13.14	8.67	13.21	4.77	7.46	31.39	38.00	1.27	7.10	3.20
Sr	304.41	159.20	226.74	208.05	153.05	96.58	176.53	172.33	171.38	219.15	240.10	154.40	148.16	105.65	148.61	107.40
Ba	174.24	80.75	187.35	160.98	27.47	16.74	35.58	48.10	34.24	40.00	39.08	117.60	77.32	34.51	46.94	38.42
Y	39.17	44.40	30.96	32.21	17.66	17.79	31.76	34.55	32.52	29.84	29.51	29.63	29.10	30.77	29.55	30.79
Zr	165.34	190.37	122.84	125.89	71.69	73.98	153.01	157.41	138.20	138.26	136.87	118.48	111.8	117.95	114.89	115.69
Hf	4.44	5.12	3.34	3.33	1.75	1.78	4.06	4.22	3.79	3.53	3.46	3.24	2.95	3.16	3.18	3.08
Nb	4.48	5.15	3.38	3.50	1.81	1.80	3.76	3.78	3.64	2.59	2.56	2.37	2.85	3.15	3.07	2.80
Ta	0.31	0.36	0.23	0.23	0.14	0.14	0.23	0.27	0.24	0.18	0.17	0.16	0.16	0.18	0.18	0.15
Pb	2.59	2.70	3.50	2.97	0.95	2.20	1.25	1.22	1.11	1.06	1.09	0.99	1.15	1.06	1.17	1.04
Th	1.00	0.95	0.47	0.49	0.30	0.31	1.15	1.55	1.14	0.15	0.14	0.08	0.04	0.05	0.05	0.04
U	0.32	0.30	0.17	0.18	0.19	0.19	0.59	0.68	0.52	0.12	0.21	0.08	0.01	0.09	0.07	0.02
ΣREE	87.72	98.72	68.17	68.84	40.89	41.42	70.71	75.47	72.22	60.84	58.75	54.38	55.49	59.47	57.88	56.27
(La/Yb)N	1.47	1.33	1.27	1.24	1.72	1.77	1.39	1.47	1.44	1.06	1.06	0.93	1.00	1.10	1.14	0.94
Eu*	0.92	0.85	0.91	0.95	0.73	0.73	0.85	0.83	0.86	0.94	0.95	0.92	0.96	0.98	1.00	0.88

Table 1. Continued.

samples	Olivine gabbros				Massive gabbros		Hornblende gabbros			Group 1 basalts						
	LYB17-4	LYB18-1	LYB18-4	LYB18-6	9LY04-1	9LY04-3	DQ43-1	DQ43-2	DQ43-8	9LY03-2	9LY03-6	DQ42-6	DQ42-9	DQ53-1	DQ53-3	DQ56
(La/Sm)N	1.11	0.96	0.93	0.91	1.34	1.35	1.09	1.15	1.10	0.81	0.82	0.75	0.74	0.81	0.83	0.73
(Gd/Yb)N	1.21	1.30	1.25	1.25	2.51	2.51	1.10	1.16	1.12	1.19	1.17	1.17	1.21	1.22	1.22	1.17
Zr/Y	4.22	4.29	3.97	3.91	4.06	4.16	4.82	4.56	4.25	4.63	4.64	4.00	3.84	3.83	3.89	3.76
Ti/Y	305.17	335.49	338.34	343.53	685.59	684.10	224.55	242.59	246.97	329.81	330.48	316.92	328.94	348.89	350.68	331.12
Th/Yb	0.23	0.20	0.13	0.14	0.16	0.17	0.31	0.41	0.31	0.04	0.04	0.02	0.01	0.02	0.01	0.01
Ta/Yb	0.07	0.07	0.07	0.07	0.08	0.08	0.06	0.07	0.07	0.05	0.05	0.05	0.05	0.06	0.06	0.04
Nb/Y	0.11	0.12	0.11	0.11	0.10	0.10	0.12	0.11	0.11	0.09	0.09	0.08	0.10	0.10	0.10	0.09
Nb/Zr	0.03	0.03	0.03	0.03	0.03	0.02	0.02	0.02	0.03	0.02	0.02	0.02	0.03	0.03	0.03	0.02
U/Th	0.32	0.32	0.35	0.36	0.62	0.60	0.51	0.44	0.45	0.81	1.53	0.99	0.21	1.76	1.62	0.53
Ba/Th	175.11	85.18	401.17	327.20	91.70	54.54	30.83	31.07	30.00	273.97	279.12	1547.39	2034.61	676.65	1043.04	1067.08

samples	Group 2 basalts													Group 3 basalts									
	9LY05-1	9LY05-2	9LY05-3	LY01	LY03	LY4	LY6	LY07	DQ52-8	LY12	LY13	LY17	LY21	06HS02-5	06HS07-6	06HS07-7	DQ40-5	DQ45-4	DQ45-6	DQ41-5	DQ41-8	DQ44-6	DQ44-8
SiO_2	49.46	49.46	47.66	46.96	50.00	47.50	47.98	47.53	48.62	48.28	48.13	47.97	47.86	47.65	50.89	49.09	52.14	48.43	51.93	48.11	48.52	50.36	49.50
TiO_2	2.00	2.00	1.95	2.01	2.01	2.03	2.04	2.02	2.01	1.97	1.91	1.92	1.96	2.29	2.06	2.19	3.55	2.71	2.47	2.18	2.10	2.60	2.64
Al_2O_3	15.13	15.13	14.93	15.72	14.36	15.24	14.98	14.89	14.81	14.33	15.52	15.76	15.28	15.39	14.97	14.45	11.61	13.92	13.28	15.23	15.6	13.31	13.52
TFe_2O_3	10.52	10.52	10.59	12.45	11.32	12.70	12.76	12.65	11.71	12.29	11.31	11.22	11.30	11.53	10.95	11.21	14.91	14.48	12.99	12.04	11.70	13.66	13.85
MnO	0.16	0.16	0.18	0.19	0.16	0.16	0.17	0.16	0.18	0.18	0.18	0.18	0.17	0.17	0.20	0.21	0.21	0.20	0.19	0.17	0.18	0.18	0.19
MgO	5.85	5.85	6.55	6.83	6.26	6.58	6.23	6.80	6.82	7.02	6.94	7.19	7.09	6.81	6.36	6.36	4.07	4.81	4.10	6.51	6.46	4.95	5.01
CaO	9.76	9.76	10.35	8.78	8.30	7.45	8.10	8.91	10.18	8.91	10.19	9.48	10.89	9.20	6.60	9.00	6.46	7.32	7.84	10.20	9.87	8.07	7.88
Na_2O	3.79	3.79	3.58	3.39	4.46	4.53	4.29	3.81	2.54	3.85	2.59	2.64	2.63	2.93	4.08	3.94	6.09	5.24	5.61	3.07	2.99	3.34	4.60
K_2O	0.81	0.81	0.55	0.68	0.69	0.31	0.52	0.39	0.31	0.29	0.74	0.80	0.48	0.46	0.23	0.12	0.09	0.24	0.15	0.46	0.49	1.00	0.52
P_2O_5	0.25	0.25	0.24	0.18	0.21	0.18	0.18	0.18	0.24	0.18	0.21	0.22	0.21	0.33	0.33	0.34	0.49	0.36	0.34	0.24	0.24	0.34	0.36
LOI	2.00	2.00	3.02	2.35	1.92	2.70	2.32	2.38	2.10	2.43	2.03	2.31	1.93	2.9	2.95	2.63	0.73	1.93	1.28	1.45	1.53	1.72	1.65
Total	99.73	99.73	99.60	99.55	99.70	99.38	99.57	99.72	99.51	99.72	99.75	99.69	99.80	99.66	99.62	99.55	100.35	99.64	100.18	99.66	99.69	99.53	99.72
Mg no.	52	52	55	52	52	51	49	52	54	53	55	56	55	54	53	53	35	40	38	52	52	42	42
La	7.96	7.67	7.69	5.49	6.94	5.67	6.13	5.17	8.05	5.47	8.17	8.15	8.41	13.18	12.76	13.46	13.81	15.92	14.61	8.76	8.51	13.99	15.10
Ce	22.61	22.33	22.01	15.68	18.88	16.25	17.33	14.89	22.52	16.72	21.95	23.43	21.78	34.32	32.71	34.82	37.13	40.66	37.11	24.64	23.8	36.61	39.78
Pr	3.66	3.50	3.45	2.59	2.93	2.66	2.83	2.46	3.48	2.67	3.40	3.54	3.37	4.89	4.72	4.99	5.79	6.20	5.69	3.81	3.71	5.71	6.20
Nd	18.29	17.3	17.68	13.32	14.25	13.73	14.34	13.01	17.81	13.87	16.53	17.51	16.16	21.60	21.18	22.55	28.77	29.44	27.11	18.77	18.19	27.76	30.26
Sm	5.57	5.25	5.19	4.32	4.36	4.46	4.66	3.92	5.27	4.43	5.01	5.11	4.89	5.88	5.49	5.95	8.36	8.49	7.83	5.52	5.44	8.14	8.84
Eu	1.70	1.66	1.62	1.53	1.58	1.54	1.66	1.47	1.77	1.46	1.57	1.52	1.51	1.93	1.77	1.97	2.67	2.96	2.53	1.77	1.8	2.44	2.40
Gd	6.41	6.26	6.18	5.28	5.51	5.46	5.86	5.07	6.38	5.72	5.86	6.34	5.36	6.40	5.98	6.43	9.98	10.10	9.22	6.59	6.42	9.41	10.23
Tb	1.17	1.15	1.13	1.01	1.02	0.99	1.05	0.94	1.19	0.99	1.07	1.10	0.97	1.08	1.06	1.11	1.83	1.79	1.65	1.22	1.19	1.72	1.89
Dy	7.90	7.59	7.51	6.67	6.73	6.64	7.01	6.3	7.47	6.54	7.05	6.94	6.32	6.67	6.71	7.03	12.12	11.79	10.77	8.00	7.88	11.61	12.44
Ho	1.69	1.66	1.62	1.42	1.52	1.43	1.50	1.37	1.65	1.40	1.47	1.50	1.31	1.39	1.41	1.51	2.58	2.48	2.29	1.70	1.70	2.49	2.73
Er	4.53	4.49	4.33	4.00	4.25	3.94	4.07	3.88	4.46	3.87	3.99	4.15	3.64	3.79	3.84	4.13	6.97	6.83	6.29	4.66	4.65	6.93	7.64
Tm	0.66	0.67	0.64	0.59	0.63	0.58	0.59	0.59	0.67	0.59	0.59	0.60	0.54	0.56	0.56	0.59	1.02	1.01	0.92	0.71	0.71	1.04	1.13
Yb	4.11	4.26	4.19	3.69	3.75	3.66	3.80	3.45	4.30	3.73	3.74	3.96	3.48	3.47	3.47	3.82	6.42	6.27	5.68	4.43	4.44	6.68	7.20
Lu	0.62	0.67	0.68	0.55	0.54	0.56	0.58	0.51	0.62	0.55	0.57	0.59	0.53	0.53	0.53	0.58	0.97	0.95	0.85	0.65	0.67	1.01	1.10
Sc	40.62	40.00	39.88	39.95	38.80	40.91	45.16	39.36	39.39	39.10	48.63	37.13	41.46	34.41	31.69	33.26	34.74	44.88	41.62	40.68	39.75	43.82	43.78
V	300.39	291.39	282.33	320.1	308.4	311.16	318.12	302.47	267.1	301.38	291.54	278.28	273.26	300.82	286.39	293.97	343.49	319.83	298.59	295.25	289.05	288.74	295.97
Cr	252.38	257.11	243.73	249.85	253.2	251.32	250.48	250.23	225.53	266.17	232.96	238.96	232.51	225.17	168.44	184.17	95.92	60.72	55.37	223.82	228.2	54.23	56.25
Co	39.09	44.13	39.43	45.55	39.25	43.27	44.60	42.14	36.77	43.51	40.09	39.65	38.93	38.01	34.63	33.97	31.29	35.94	31.03	40.07	40.16	30.63	32.08
Ni	68.25	81.46	73.73	87.07	77.19	83.47	83.10	83.64	71.14	87.55	70.76	72.07	78.52	86.06	74.47	69.25	20.66	26.70	23.20	66.97	70.05	24.59	36.94
Ga	17.52	17.34	17.50	18.12	16.74	16.09	17.49	16.90	19.84	16.91	18.45	17.43	17.82	20.07	18.28	18.99	17.19	21.71	20.46	19.16	19.41	20.04	21.77
Cs	0.62	0.94	0.84	0.78	0.49	0.21	0.26	0.55	0.52	0.42	0.54	0.86	0.51	0.56	0.39	0.39	0.54	0.08	0.08	0.64	0.86	0.28	0.18
Rb	24.66	1.36	15.02	16.01	11.25	7.52	13.88	11.74	6.20	4.95	14.64	13.21	9.70	4.94	2.89	0.15	0.12	5.45	3.61	4.62	4.98	22.3	10.55
Sr	262.12	200.79	259.46	184.29	174.88	181.06	182.85	183.51	170.86	180.34	176.68	165.45	186.49	332.57	208.96	288.39	115.73	141.82	127.35	191.58	192.42	211.33	218.33

Table 1. Continued.

	Group 2 basalts													Group 3 basalts									
samples	9LY05-1	9LY05-2	9LY05-3	LY01	LY03	LY4	LY6	LY07	DQ52-8	LY12	LY13	LY17	LY21	06HS02-5	06HS07-6	06HS07-7	DQ40-5	DQ45-4	DQ45-6	DQ41-5	DQ41-8	DQ44-6	DQ44-8
Ba	46.94	49.59	59.56	76.43	79.26	21.57	29.42	60.83	49.30	31.10	65.78	75.13	44.00	50.97	59.04	61.11	35.39	48.81	18.68	78.73	75.75	181.28	81.77
Y	38.15	38.83	37.46	34.46	35.97	32.51	34.59	33.23	40.80	34.09	35.34	35.73	34.33	33.86	33.33	35.62	59.6	60.99	56.26	40.86	40.43	57.89	61.66
Zr	154.97	185.18	178.74	134.02	148.99	118.44	118.17	131.26	168.28	119.24	152.62	158.79	147.56	209.36	179.33	224.6	270.57	278.78	255.19	202.26	202.62	253.55	277.77
Hf	3.90	4.85	4.71	3.68	4.05	3.42	3.51	3.62	4.58	3.23	4.15	4.16	3.83	4.91	4.79	5.67	7.90	7.37	6.69	5.42	5.40	7.05	7.62
Nb	4.64	4.74	4.62	2.81	3.88	2.86	2.88	2.72	4.92	2.86	4.79	4.88	4.82	8.10	7.65	8.12	7.54	7.46	6.84	5.04	5.00	6.94	7.49
Ta	0.33	0.32	0.33	0.20	0.27	0.18	0.18	0.20	0.28	0.19	0.32	0.32	0.31	0.82	0.52	0.56	0.57	0.54	0.48	0.37	0.36	0.48	0.55
Pb	1.13	1.40	1.90	1.61	1.83	1.42	1.34	1.26	1.77	1.53	2.48	1.76	1.37	3.09	1.95	2.28	2.52	2.50	2.26	1.52	1.68	1.92	1.94
Th	0.55	0.48	0.50	0.38	0.62	0.55	0.58	0.36	0.55	0.43	0.99	0.91	0.78	0.71	0.75	0.81	1.01	2.15	2.03	0.72	0.71	2.16	2.41
U	0.27	0.18	0.21	0.18	0.38	0.20	0.20	0.19	0.25	0.13	0.27	0.26	0.23	0.27	0.38	0.28	0.17	0.80	0.77	0.25	0.25	0.72	0.80
ΣREE	86.90	84.46	83.92	66.16	72.90	67.56	71.40	63.02	85.64	68.01	80.97	84.45	78.27	105.69	102.17	108.93	138.4	144.88	132.56	91.24	89.1	135.54	146.93
(La/Yb)N	1.39	1.29	1.32	1.07	1.33	1.11	1.16	1.07	1.34	1.05	1.57	1.48	1.73	2.72	2.64	2.53	1.54	1.82	1.85	1.42	1.37	1.50	1.50
Eu*	0.87	0.89	0.87	0.98	0.99	0.95	0.97	1.01	0.93	0.89	0.89	0.81	0.90	0.96	0.94	0.97	0.89	0.98	0.91	0.90	0.93	0.85	0.77
(La/Sm)N	0.92	0.94	0.96	0.82	1.03	0.82	0.85	0.85	0.99	0.80	1.05	1.03	1.11	1.45	1.50	1.46	1.07	1.21	1.20	1.02	1.01	1.11	1.10
(Gd/Yb)N	1.29	1.22	1.22	1.18	1.22	1.24	1.28	1.21	1.23	1.27	1.30	1.32	1.27	1.53	1.43	1.39	1.29	1.33	1.34	1.23	1.19	1.17	1.18
Zr/Y	4.06	4.77	4.77	3.89	4.14	3.64	3.42	3.95	4.12	3.50	4.32	4.44	4.30	6.18	5.38	6.31	4.54	4.57	4.54	4.95	5.01	4.38	4.50
Ti/Y	314.21	308.74	311.23	350.25	335.32	374.24	353.51	364.37	294.88	346.13	323.89	321.56	342.21	406.19	371.01	369.33	356.65	266.31	263.15	319.37	311.81	269.17	256.61
Th/Yb	0.13	0.11	0.12	0.10	0.16	0.15	0.15	0.10	0.13	0.11	0.26	0.23	0.22	0.20	0.21	0.21	0.16	0.34	0.36	0.16	0.16	0.32	0.34
Ta/Yb	0.08	0.08	0.08	0.05	0.07	0.05	0.05	0.06	0.06	0.05	0.09	0.08	0.09	0.24	0.15	0.15	0.09	0.09	0.09	0.08	0.08	0.07	0.08
Nb/Y	0.12	0.12	0.12	0.08	0.11	0.09	0.08	0.08	0.12	0.08	0.14	0.14	0.14	0.24	0.23	0.23	0.13	0.12	0.12	0.12	0.12	0.12	0.12
Nb/Zr	0.03	0.03	0.03	0.02	0.03	0.02	0.02	0.02	0.03	0.02	0.03	0.03	0.03	0.04	0.04	0.04	0.03	0.03	0.03	0.02	0.02	0.03	0.03
U/Th	0.50	0.36	0.42	0.48	0.61	0.36	0.35	0.52	0.46	0.31	0.27	0.28	0.29	0.39	0.51	0.35	0.17	0.37	0.38	0.34	0.35	0.33	0.33
Ba/Th	84.87	102.46	118.65	203.28	128.88	39.07	50.81	168.98	90.30	72.83	66.38	82.38	56.43	72.09	79.25	75.72	35.08	22.67	9.21	108.75	106.09	83.81	33.90

$Eu^* = 2 \times Eu_N/(Sm_N + Gd_N)$; Mg no. $= 100 \times MgO/(MgO + FeO^T)$; $FeO^T = 0.9 \times TFe_2O_3$.

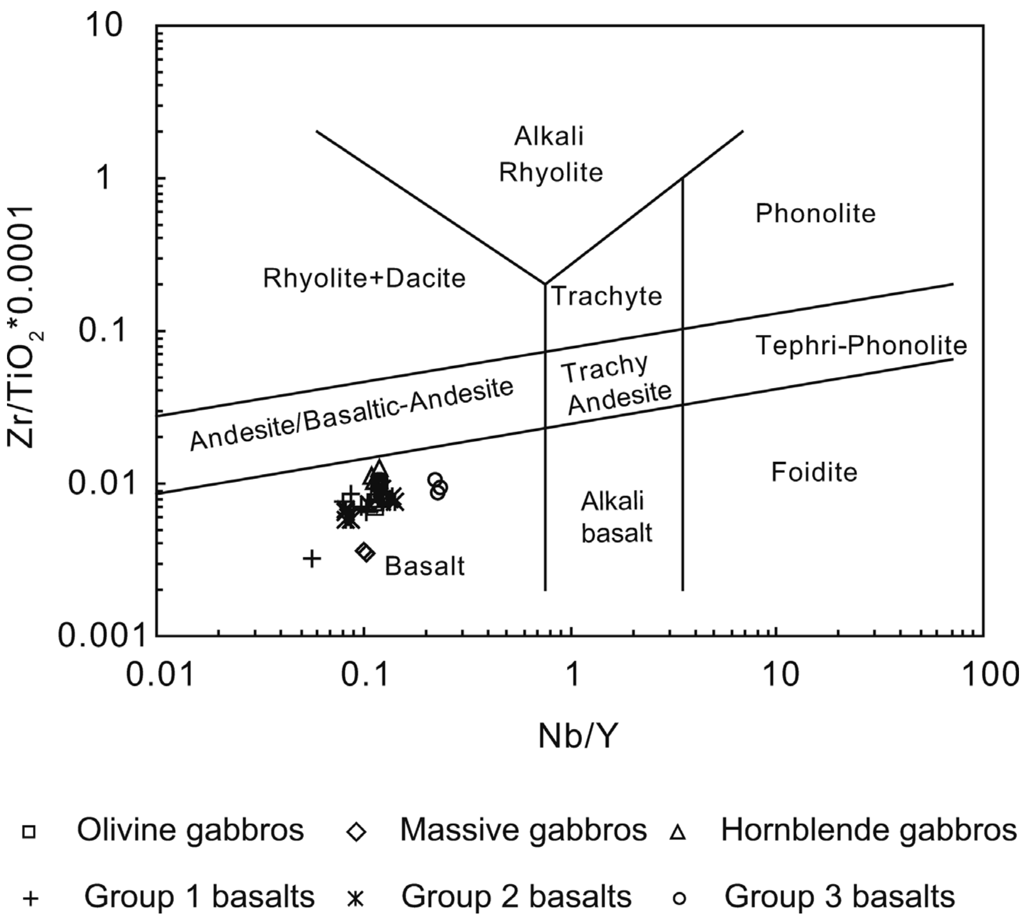

Figure 5. Zr/Ti v. Nb/Y diagram of Winchester & Floyd (1977).

$K_2O + Na_2O$ (2.9–6.2 wt %). In the Zr/Ti v. Nb/Y diagram (Winchester & Floyd, 1977), all the samples plot within the basalt fields (Fig. 5). As demonstrated by the binary diagrams (Figs 6, 7), the rocks have positive correlations between Mg no. (100 × MgO/(MgO + FeOT) and Al_2O_3, CaO, Cr and Ni contents, and a negative correlation between Mg no. and TFe_2O_3, TiO_2, P_2O_5, Y and Zr contents. The mobile elements (K_2O, Rb, Ba, U and Sr) show a large range of irregular variations.

4.a. Gabbros

Geochemically, the gabbros form three types, which are consistent with those defined petrologically above (Table 1; Figs 5, 6, 7).

The massive gabbros (Type 1) and olivine gabbros (Type 2) have similar major element characteristics, which are analogous to those of the basalts (Figs 5, 6). They display a limited range of compositions, e.g. SiO_2 46.1–48.6 wt %; TiO_2 1.8–2.5 wt %; Al_2O_3 14.1–15.0 wt %; Mg no. 46–56. The massive gabbros have relatively low Ni (48 ppm) and Cr (121–129 ppm) contents and total rare earth element (REE) contents (40–41 ppm), and the HREEs are lower than those of normal mid-ocean ridge basalt (N-MORB) (Sun & McDonough, 1989). The REE patterns are slightly enriched in LREEs ($La/Yb_N = 1.6$). A weak negative Eu anomaly ($Eu/Eu^* = 0.9$) is notable (Fig. 8). The trace element ratios (Nb/Y = 0.10, Nb/Zr = 0.02–0.03, Zr/Y = 4.06–4.16 and Ta/Yb = 0.08) are similar to those of N-MORB. These gabbros display primitive mantle-normalized trace element patterns enriched in Pb and Ti elements relative to REEs, and are relatively depleted in Nb and Ta. All these features are subduction-related signatures.

Cr and Ni abundances of the olivine gabbros vary from 181 ppm to 248 ppm and 48 ppm to 65 ppm, respectively. All the REEs are slightly richer than those of N-MORB (Fig. 8; Table 1). The REEs display flat patterns ($La/Yb_N = 1.2$–1.5) and a weak negative Eu anomaly ($Eu/Eu^* = 0.8$–1.0). The trace element ratios (Nb/Y = 0.11–0.12, Nb/Zr = 0.03, Zr/Y = 3.91–4.29 and Ta/Yb = 0.07) are similar to those of N-MORB or enriched mid-ocean ridge basalt (E-MORB) (Sun & McDonough, 1989). However, subduction-related signatures are shown by depletion in Nb and Ta in primitive mantle-normalized trace element patterns.

The hornblende gabbros (Type 3) are different from the gabbros of Types 1 and 2 and the basalts (Figs 5, 6, 7). The hornblende gabbros are characterized by relatively high SiO_2 (50.0–50.3 wt %), CaO (10.2–11.4 wt %) and Al_2O_3 (14.8–16.5 wt %), and low TiO_2 (1.2–1.4 wt %) and MgO (6.6–7.9 wt %) contents. The Mg no. range is from 60 to 63. The gabbros display moderate Cr (160–166 ppm) and Ni (49–57 ppm)

https://doi.org/10.1017/S0016756811000811 Published online by Cambridge University Press

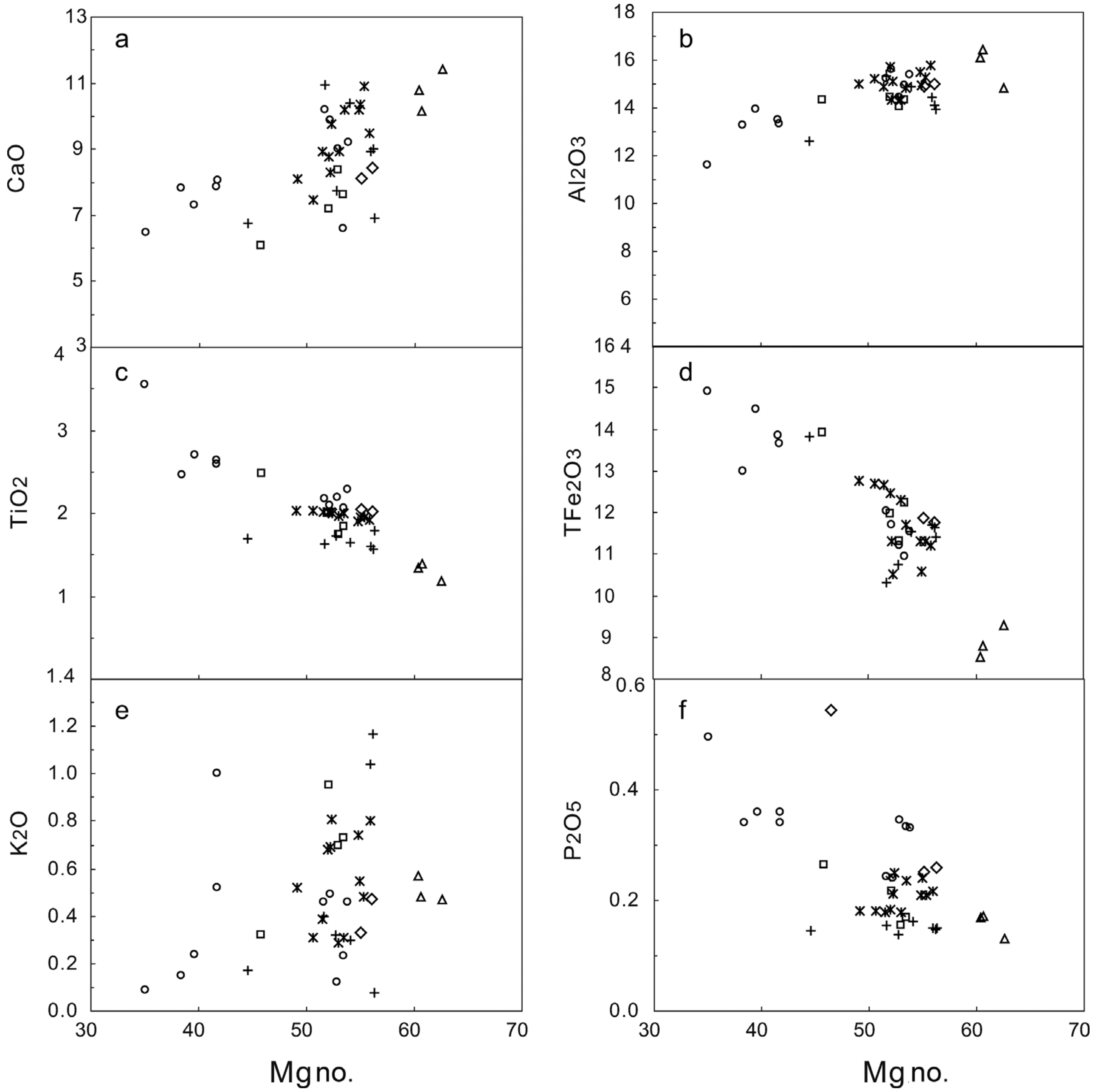

Figure 6. Mg no.–major binary diagrams versus Al_2O_3, TFe_2O_3, CaO, MnO, P_2O_5, TiO_2 for rocks from the Liuyuan complex. Values are in wt % for oxides. Symbols as in Figure 5.

contents. The REEs of the samples are slightly richer than those of N-MORB (Fig. 8; Table 1), and display flat patterns (La/Yb_N = 1.4–1.5) with a negative Eu anomaly (Eu/Eu* = 0.8–0.9). The trace element ratios (Nb/Y = 0.11–0.12, Nb/Zr = 0.02–0.03, Zr/Y = 4.25–4.82 and Ta/Yb = 0.06–0.07) range between those of N-MORB and E-MORB. Primitive mantle-normalized trace element patterns are enriched in large-ion lithophile elements (LILEs) (Rb, Ba, U, K) and Th and Pb, and depleted in Nb, Ta, Ti and Sr, which are similar to those of subduction-related magmas.

4.b. Basaltic rocks

Most basaltic samples have low loss on ignition (LOI) (<3.0 wt %), which indicates low levels of alteration, except for DQ56 (LOI = 6.25 %), which is highly altered. The basaltic rocks are characterized by a wide range of SiO_2 (47.0–52.1 wt %), TiO_2 (1.6–3.6 wt %), Al_2O_3 (11.6–15.8 wt %), MgO (4.1–7.5 wt %), TFe_2O_3 (8.5–14.9 wt %), CaO (6.5–11.0 wt %) and MnO (0.14–0.27 wt %) contents, and Mg no. is 35–56 (Table 1; Fig. 6). The values of Cr (54.2–266.2 ppm) and Ni (20.7–87.6 ppm) are close to those of MORB, and incompatible element contents are relatively high, for example Zr (111.8–278.8 ppm), Y (29.1–278.2 ppm) and Yb (1.5–7.2 ppm) (Sun & McDonough, 1989).

The basaltic rocks are clearly divisible into three different groups based on their element contents (Table 1; Fig. 6). Group 1 is characterized by the lowest TiO_2 contents (1.6–1.8 %), while Group 2 has intermediate values (1.9–2.0 %), and Group 3 basalts have

https://doi.org/10.1017/S0016756811000811 Published online by Cambridge University Press

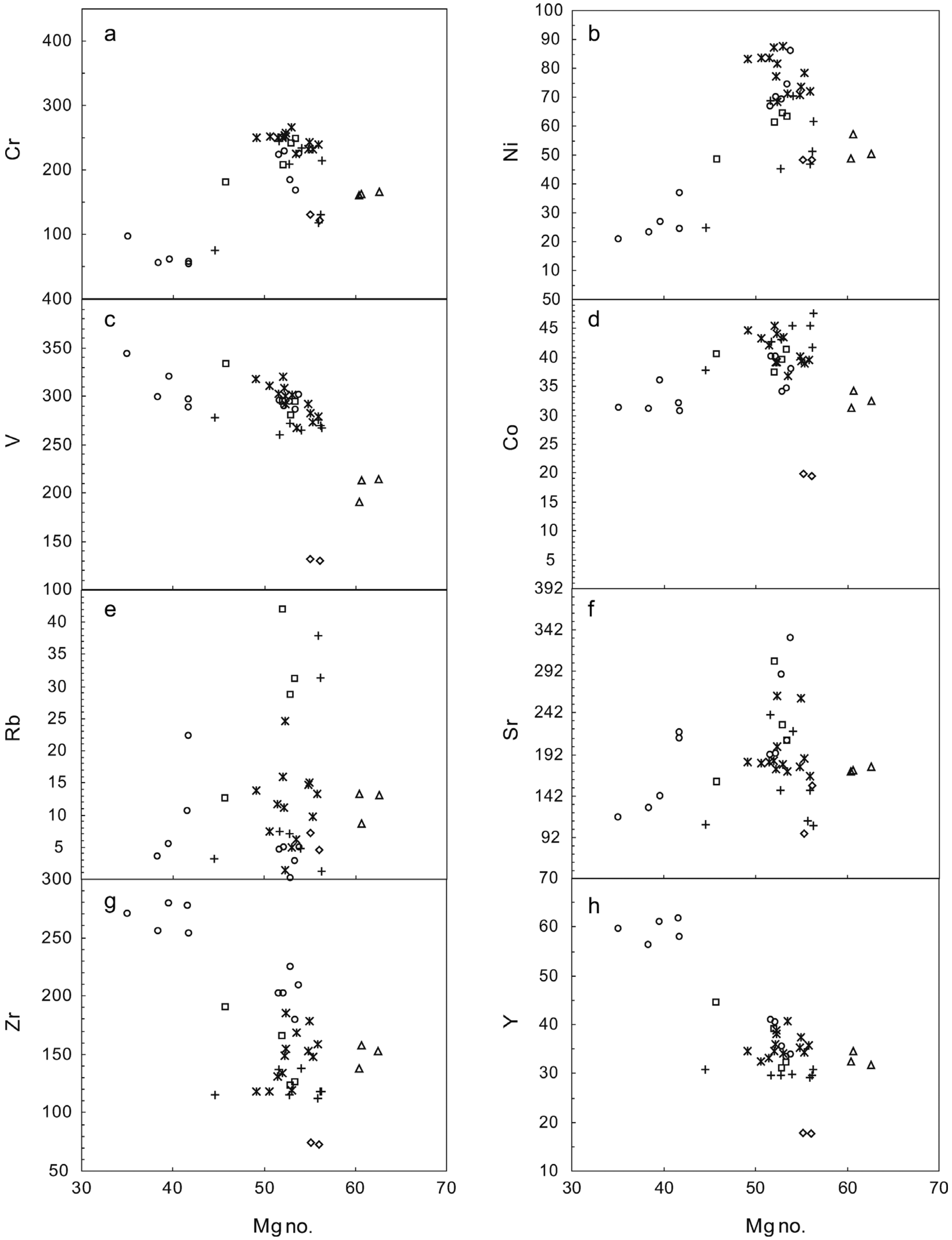

Figure 7. Mg no.–trace element binary diagrams versus Cr, Ni, V, Co, Rb, Sr, Zr, Y for rocks from the Liuyuan complex. Values are in ppm for trace elements. Symbols as in Figure 5.

the highest (2.1–3.6 %). REE, Nb, Ta, Zr, Hf and Pb contents also increase progressively from Group 1 to 3, but the low ionic potential trace elements, including Li, K, Rb, Cs, Ba, Sr, U and Pb, and Th contents are irregular, with large ranges of variation (Figs 7, 9; Table 1). Most Group 1 basalts were collected from the south,

https://doi.org/10.1017/S0016756811000811 Published online by Cambridge University Press

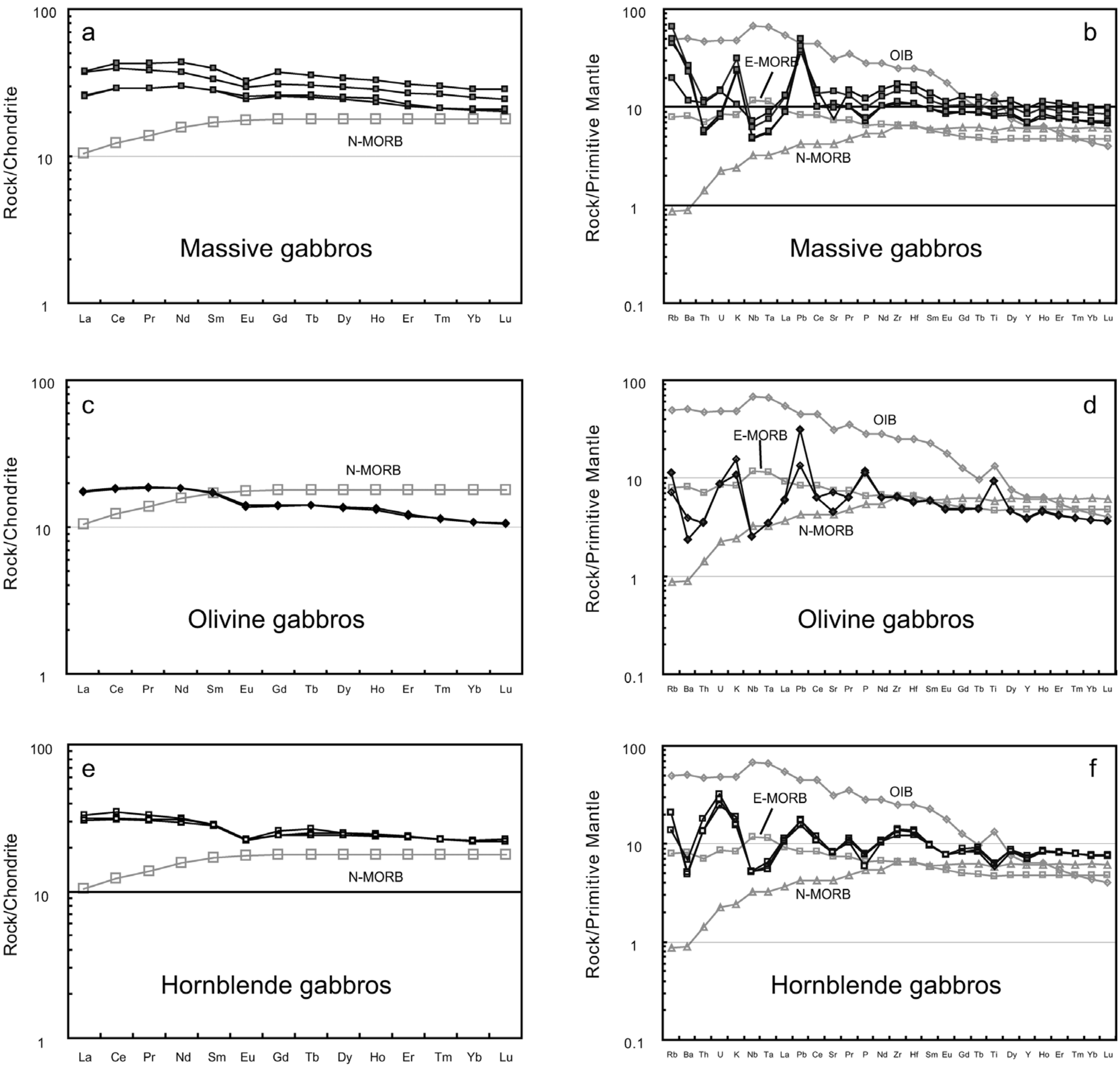

Figure 8. Chondrite-normalized REE patterns and primitive mantle (PM)-normalized multi-element diagrams for gabbros from the Liuyuan complex. The chondrite values are from Boynton (1984). The PM, N-MORB, E-MORB and OIB values are from Sun & McDonough (1989).

Group 2 basalts from the middle, and Group 3 basalts from the north of the LC.

Group 1 basalts have similar REE patterns to N-MORB (Fig. 9a) with a typical flat to weakly depleted pattern (La/Yb_N = 0.9–1.1) (Fig. 9a). They have a weak negative Eu anomaly (Eu/Eu^* = 0.9–1.0) and symmetrical LREE-depleted patterns (La/Sm_N = 0.7–0.8) with flat HREEs (Gb/Yb_N = 1.2). They have similar low Th/Yb (0.01–0.04), Ta/Yb (0.04–0.06), Nb/Y (0.08–0.10) and Nb/Zr (0.02–0.03) ratios to N-MORB, but high Zr/Y (3.76–4.64) and Ti/Y (317–351) ratios close to E-MORB. In the primitive mantle-normalized trace element diagram (Fig. 9b), this group of basalts displays depletions in Nb, Ta and Th relative to LILEs and REEs, and Pb enrichment. LILEs (Rb, Ba, U and Sr) vary from enriched to depleted. These characteristics are similar to those of supra-subduction zone (SSZ) ophiolites (Hawkins, 1994, 2003; Hoeck *et al*. 2002; Dilek & Furnes, 2011).

Group 2 basalts display REE patterns similar to those of E-MORB with a slight enrichment in LREEs (La/Yb_N = 1.1–1.7), and an overall REE enrichment 1.2–2.5 times that of typical E-MORB (Fig. 9c). The basalts have higher Th/Yb (0.1–0.26), Ta/Yb (0.05–0.09) and Nb/Y (0.08–0.14) ratios than the Group 1 basalts, and low Nb/Zr (0.02–0.03) ratios, which plot between N-MORB and E-MORB (Sun & McDonough, 1989). Zr/Y and Ti/Y ratios vary from 3.42 to 4.77 and 295 to 374, respectively. On a primitive mantle-normalized trace element diagram (Fig. 9d), the Group 2 basalts also exhibit an enrichment in LILEs (Rb, Ba, K and U) and Pb, and depletion in Nb, Ta and Th relative to LILEs and REEs, and thus are similar to subduction-related magmas.

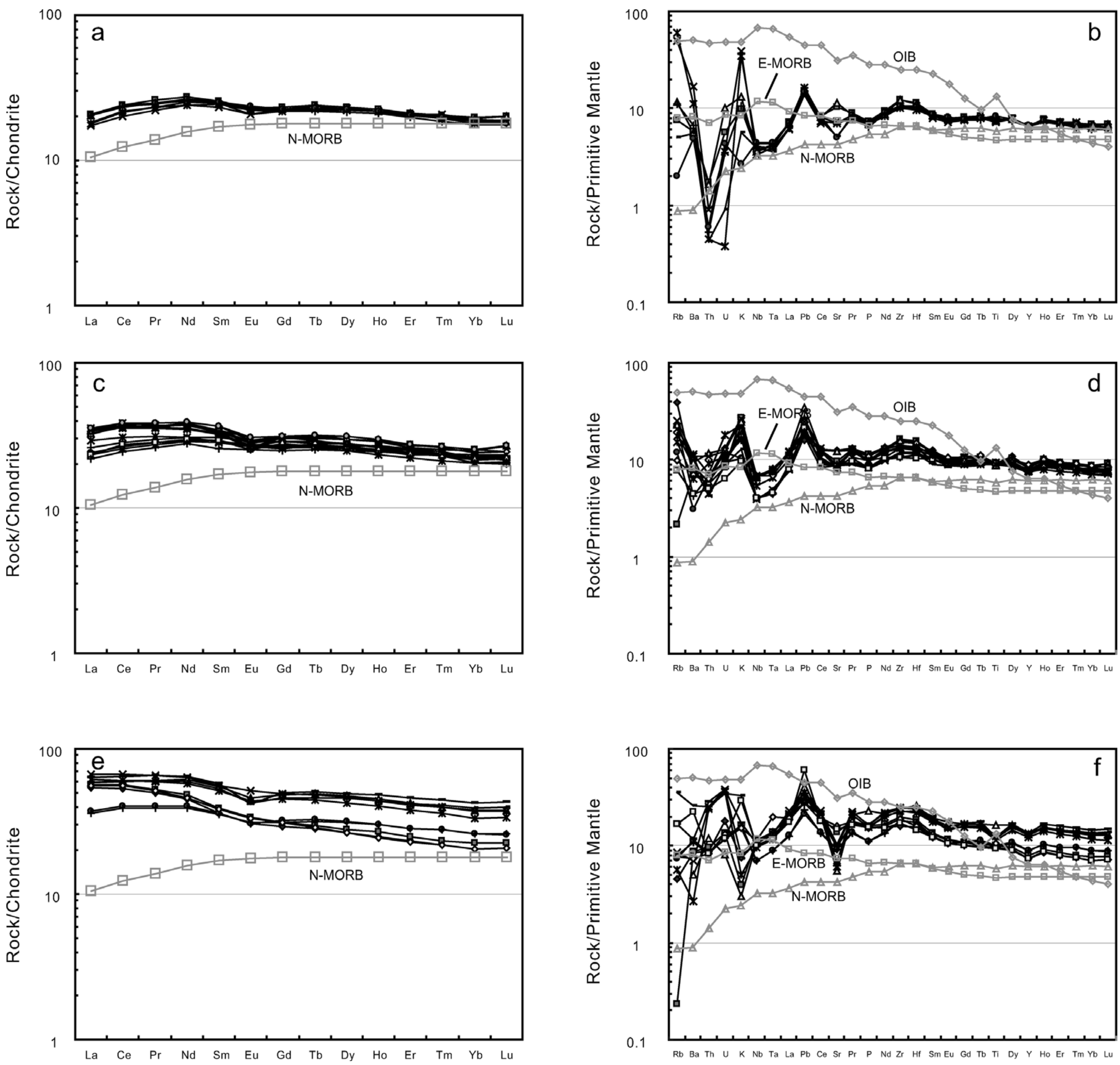

Figure 9. Chondrite-normalized REE patterns and primitive mantle (PM)-normalized multi-element diagrams for the three groups of basalts from the Liuyuan complex. The chondrite values are from Boynton (1984). The PM, N-MORB, E-MORB and OIB values are from Sun & McDonough (1989).

Group 3 basalts are the most trace element-enriched of the three basalt groups. They are slightly LREE-enriched ($La/Yb_N = 1.4–2.7$), and have weak negative Eu anomalies ($Eu/Eu^* = 0.8–1.0$) (Fig. 9e). They exhibit the highest Th/Yb (0.16–0.36), Ta/Yb (0.07–0.24), Nb/Y (0.12–0.24) and Nb/Zr (0.02–0.04) ratios, which are between those of N-MORB and E-MORB. They have Zr/Y (4.38–6.31) and Ti/Y (257–406) ratios that are between those of MORB and ocean island basalt (OIB) (Sun & McDonough, 1989). These subduction-related signatures are also confirmed by trace elements with relative depletion in Sr and high-field-strength elements (HFSEs) (Nb, Ta and Ti), and enrichments in Pb, LILEs and REEs on a primitive mantle-normalized trace element diagram (Fig. 9f).

5. Isotopic determinations

Rb–Sr and Sm–Nd isotopic results for the LC are presented in Table 2. Sr initial ratios and $\varepsilon_{Nd(t)}$ values are calculated at an age of 280 Ma, which is the same as that obtained from zircon geochronology of a gabbro presented in Section 6. The massive gabbros and olivine gabbros have similar $\varepsilon_{Nd(t)}$ values of 6.9 and 6.7–7.5, respectively. They exhibit relatively high $(^{87}Sr/^{86}Sr)_i$ values of 0.7057 and 0.7088–0.7098, respectively. The hornblende gabbros have moderate $\varepsilon_{Nd(t)}$ (7.7) and the lowest $(^{87}Sr/^{86}Sr)_i$ (0.7034) values, which plot in the mantle array magma area (Fig. 10).

The basaltic samples exhibit relatively low $(^{87}Sr/^{86}Sr)_i$ isotopic ratios varying between 0.703662 and 0.704327, and high $(^{143}Nd/^{144}Nd)_i$ isotopic ratios varying between 0.5126 and 0.5127. They have positive

https://doi.org/10.1017/S0016756811000811 Published online by Cambridge University Press

Table 2. Sm–Nd and Rb–Sr isotopic data from the Liuyuan complex, Beishan orogen, NW China

Rock types	Samples	Rb	Sr	$^{87}Rb/^{86}Sr$	$^{87}Sr/^{86}Sr$	2σ	$(^{87}Sr/^{86}Sr)_i$	$\varepsilon_{Sr(t)}$	Sm	Nd	$^{147}Sm/^{144}Nd$	$^{143}Nd/^{144}Nd$	(2σ)	$(^{143}Nd/^{144}Nd)_i$	$\varepsilon_{Nd(t)}$
Olivine gabbros	LYB17-4	40.28	314.3	0.3709	0.711303	0.000013	0.709825	80.3	5.02	16.47	0.1843	0.512958	0.000013	0.512620	6.7
	LYB18-4	27.56	238.6	0.3343	0.710145	0.000014	0.708813	65.9	3.87	12.35	0.1893	0.513010	0.000013	0.512663	7.5
Massive gabbros	9LY04-1	7.70	330.0	0.0675	0.705922	0.000014	0.705653	21.1	5.24	17.80	0.1778	0.512957	0.000013	0.512631	6.9
Hornblende gabbros	DQ43-8	11.53	176.1	0.1895	0.704105	0.000011	0.703350	−11.7	4.15	13.58	0.1846	0.513010	0.000014	0.512672	7.7
Group 1 basalts	9LY03-2	11.43	238.0	0.1389	0.704216	0.000013	0.703662	−7.2	3.99	12.59	0.1917	0.513091	0.000013	0.512739	9.0
	DQ42-6	30.02	154.6	0.5616	0.705955	0.000015	0.703717	−6.4	3.51	10.60	0.2003	0.513096	0.000012	0.512729	8.8
	DQ53-3	8.09	144.7	0.1617	0.704589	0.000012	0.703944	−3.2	37.55	116.5	0.1948	0.513072	0.000010	0.512715	8.5
Group 2 basalts	LY01	17.28	197.9	0.2525	0.704911	0.000013	0.703906	−3.8	4.46	13.72	0.1965	0.513017	0.000013	0.512657	7.4
	9LY05-3								5.23	17.17	0.1839	0.512992	0.000013	0.512655	7.4
	9LY05-5	4.12	148.9	0.0801	0.704531	0.000012	0.704212	0.6	5.03	16.60	0.1831	0.513002	0.000011	0.512666	7.6
	DQ52-5	6.36	211.2	0.0871	0.704197	0.000013	0.703849	−4.6	5.76	18.49	0.1882	0.512994	0.000011	0.512650	7.3
Group 3 basalts	DQ40-5	0.51	113.6	0.0129	0.704287	0.000010	0.704235	0.9	8.43	28.18	0.1808	0.512999	0.000013	0.512668	7.6
	DQ41-5	5.50	204.3	0.0778	0.704050	0.000013	0.703740	−6.1	35.38	183.1	0.1168	0.512988	0.000013	0.512655	7.4
	DQ44-6	20.89	213.9	0.2826	0.705416	0.000014	0.704290	1.7	7.68	26.10	0.1780	0.512954	0.000014	0.512628	6.8
	DQ44-8	8.75	207.1	0.1222	0.704531	0.000010	0.704044	−1.8	7.79	26.51	0.1775	0.512939	0.000013	0.512613	6.6
	DQ45-4	3.20	138.3	0.0669	0.704594	0.000012	0.704327	2.2	8.31	28.68	0.1751	0.512959	0.000013	0.512638	7.0

$\varepsilon_{Nd(t)}$ values from 6.6 to 9.0. In an $\varepsilon_{Nd(t)}$ versus $^{87}Sr/^{86}Sr$ diagram (Fig. 10), most samples fall close to, but on the high $^{87}Sr/^{86}Sr$ side of the mantle array (Tejada *et al.* 1996; Neal, Mahoney & Chazey, 2002). The Sr–Nd isotopic ratios also vary in an orderly manner between the three groups of basalts (Fig. 10; Table 2). Group 1 basalts display the highest $\varepsilon_{Nd(t)}$ (8.5–9) and lowest $(^{87}Sr/^{86}Sr)_i$ (0.703662–0.703944) isotopic ratios; the Group 2 basalts have intermediate $\varepsilon_{Nd(t)}$ (7.3–7.6) and $(^{87}Sr/^{86}Sr)_i$ (0.703849–0.704212) isotopic ratios; and the Group 3 basalts exhibit the lowest $\varepsilon_{Nd(t)}$ (6.6–7.6) and highest $(^{87}Sr/^{86}Sr)_i$ (0.70374–0.704327) isotopic ratios.

In summary, the rocks have a narrow range in positive $\varepsilon_{Nd(t)}$ values. Most samples have a narrow range in $^{87}Sr/^{86}Sr$ and these plot close to, but to the left of the mantle array, consistent with a fore-arc and/or back-arc and/or an oceanic arc setting.

6. Geochronology

In order to determine the age of the LC, zircons were separated from a hornblende gabbro (sample DQ43). The zircons are mostly colourless, transparent and well crystallized with short prismatic shapes (elongation ratios vary from 1.25 to 1.5), with grain sizes ranging from 100 to 200 μm in diameter. Cathodoluminescence (CL) images show that the zircons have similar compositions and typical basic magmatic zonal patterns (Fig. 11). These characteristics indicate that the zircons are of magmatic origin. U–Pb laser ablation (LA)-ICP-MS analytical results from 20 grains are listed in Table 3 and presented in Figure 12. The ^{206}Pb–^{238}U ages range from 281 ± 4 Ma to 296 ± 5 Ma, and concentrate in a small area close to or on the concordia line (Fig. 12a, b). Twenty analysed samples yield a ^{206}Pb–^{238}U weighted average age of 286 ± 2 Ma (MSWD = 0.62) (Fig. 12a), which is interpreted as the crystallization age of the gabbro.

7. Discussion

7.a. The origin of the Liuyuan complex

Although most of the different rock types in the LC are mutually juxtaposed by thrusts, the original stratigraphy of the ultramafic–mafic complex can be rebuilt as follows (Fig. 13): from bottom to top, ultramafic rocks, olivine gabbro, massive basalt, pillow basalt, basaltic breccia and chert with tuff beds. The basalts and gabbros share similar chemical characteristics (Figs 6, 7). They have positive correlations between Mg no. and major (Al_2O_3 and CaO) and trace elements (Cr, Ni and Co), and a negative correlation between Mg no. and major elements (TFe_2O_3, TiO_2 and P_2O_5), trace elements (Zr, Y, Nb, Ta, Hf, Pb) and REEs (Figs 6, 7; Table 1). All these values indicate that the basalts and gabbros were derived from the same source and that fractionation was important in their generation, for

https://doi.org/10.1017/S0016756811000811 Published online by Cambridge University Press

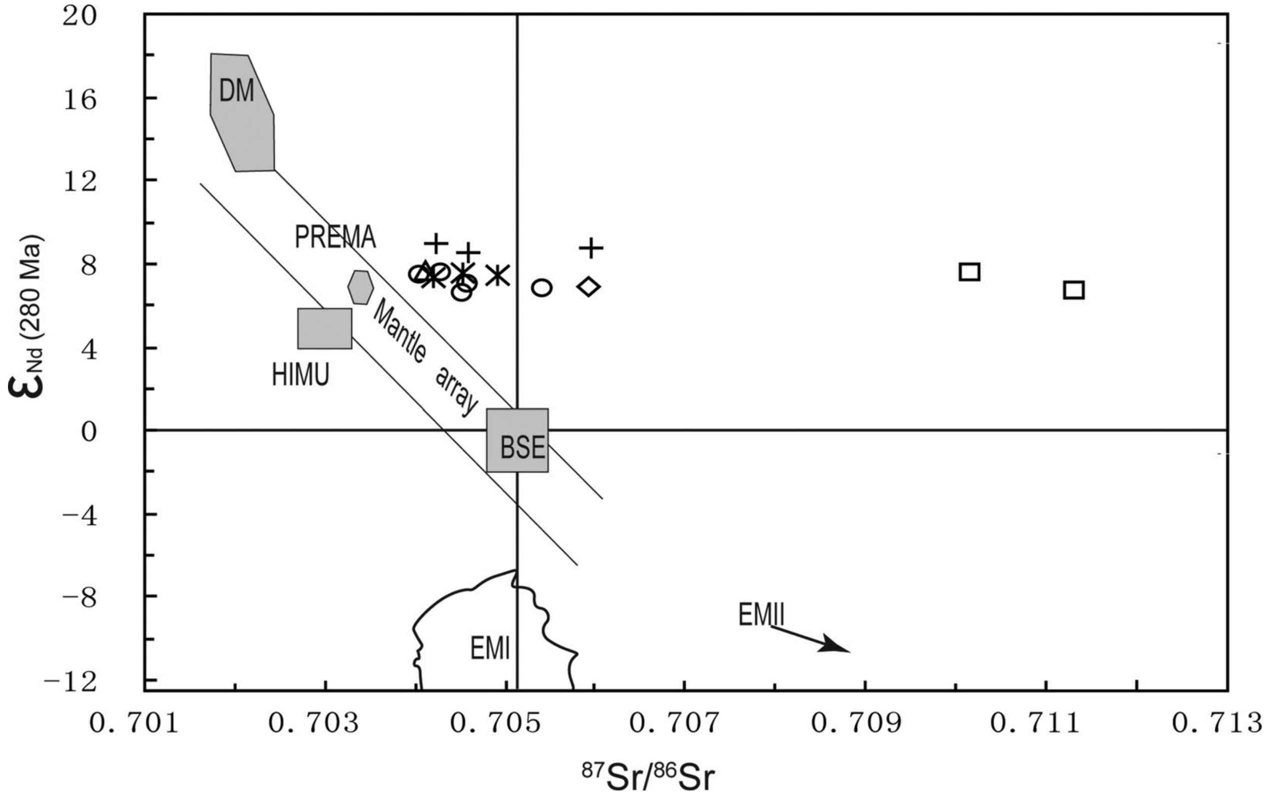

Figure 10. $\varepsilon_{Nd(t)}$ versus $^{87}Sr/^{86}Sr$ of samples from the Liuyuan complex. DM – depleted mantle; BSE – bulk silicate earth; EMI and EMII – enriched mantle; HIMU – mantle with high U/Pb ratio; PREMA – frequently observed prevalent mantle composition (Zindler & Hart, 1986).

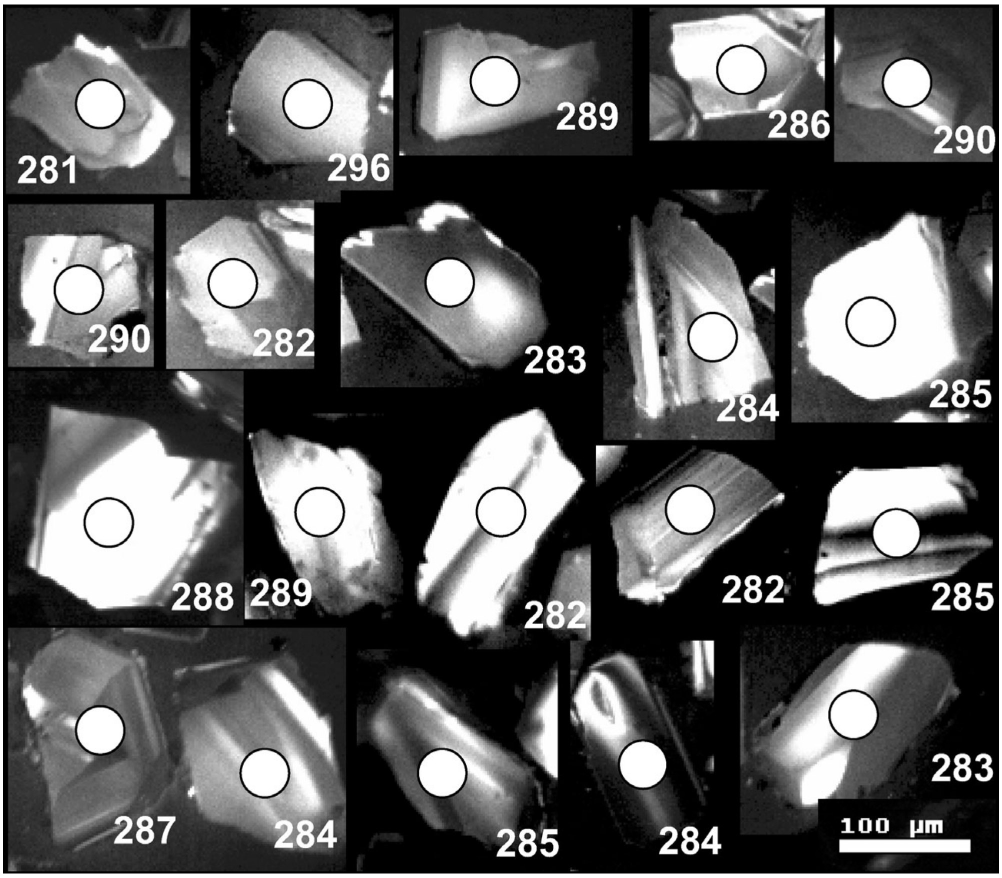

Figure 11. Cathodoluminescence (CL) images of zircons selected for radiometric dating from a hornblende gabbro in the Liuyuan complex. Circles mark the beam positions of the isotopic analyses.

https://doi.org/10.1017/S0016756811000811 Published online by Cambridge University Press

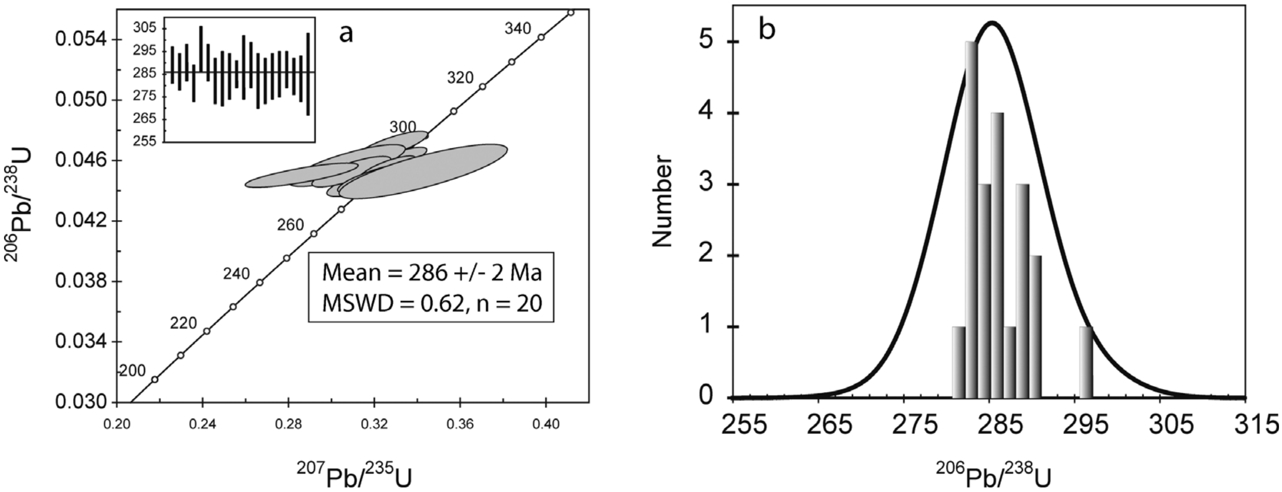

Figure 12. Concordia U–Pb diagram (a) and $^{206}Pb/^{238}U$ cumulative probability diagram (b) of LA-ICP-MS analyses of zircons from hornblende gabbros in the Liuyuan complex.

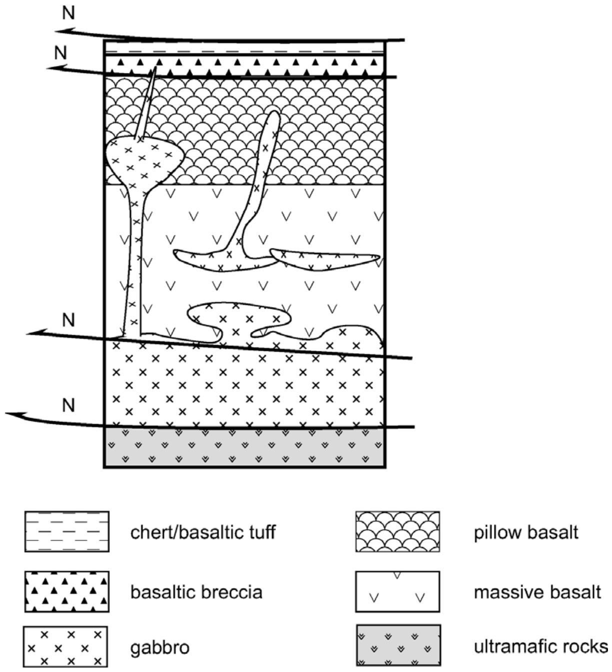

Figure 13. A reconstructed stratigraphy of the main units of the Liuyuan complex.

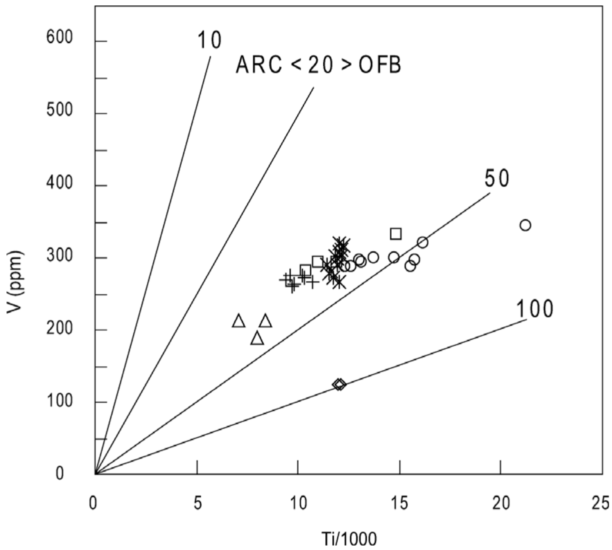

Figure 14. A Ti v. V discrimination diagram for rocks from the Liuyuan complex (Shervais, 1982). Symbols as in Figure 5. OFB – ocean floor basalt.

example the fractionation of clinopyroxene, ilmenite and plagioclase.

All the rocks display relatively high TiO_2 (1.2–3.6 wt %) contents, which are different from those of island arc magmas. The rocks exhibit an overall HREE enrichment 1.2 to 4 times that of typical N-MORB/E-MORB (Table 1; Figs 8, 9), indicating that the source of the LC was most likely a relatively fertile mantle. The relatively flat chondrite-normalized REE patterns are similar to those of N-MORB and E-MORB, and the primitive mantle-normalized trace element patterns are similar to those of basalts from SSZ ophiolites. Such a subduction-related signature is consistent with the systematic enrichments in LILEs (Rb, K, Ba, U), Th and Pb, and depletions in Nb and Ta (Hawkins, 1994, 2003; Karsten, Klein & Sherman, 1996; Hoeck *et al.* 2002).

HFSE abundances and element ratios are the most useful chemical signatures likely to be preserved, even if rocks are altered, or have undergone low-grade regional metamorphism or subduction metamorphism (Bedard, 1999). The Th/Yb, Ta/Yb, Nb/Y and Nb/Zr ratios of the three groups of basalts indicate that they vary from those of N-MORB to E-MORB, and the high Zr/Y and Ti/Y ratios vary between those of MORB and OIB (Sun & McDonough, 1989).

Several classification schemes provide diagnostic parameters to evaluate tectonic settings, of which the Ti/V ratio is one of the most useful (Shervais, 1982). On a Ti v. V diagram most Liuyuan samples plot within the ocean floor basalt (OFB) field, and exhibit a positive correlation from the MORB to the OFB fields (Fig. 14). On a Cr v. Y diagram (Fig. 15) (Pearce *et al.* 1981) most

Table 3. Zircon U–Pb LA-ICP-MS data for zircon grains from hornblende gabbros in the Liuyuan complex

	Element contents (ppm) and ratio				Isotopic ratio						Isotopic age (Ma)					
Sample	Pb(t)	Th	U	Th/U	$^{207}Pb/^{206}Pb$	1σ	$^{207}Pb/^{235}U$	1σ	$^{206}Pb/^{238}U$	1σ	$^{207}Pb/^{206}Pb$	1σ	$^{207}Pb/^{235}U$	1σ	$^{206}Pb/^{238}U$	1σ
DQ43 01	21	259	387	0.67	0.32703	0.00902	0.04592	0.00060	0.01480	0.00030	270	39	287	7	289	4
DQ43 02	42	698	720	0.97	0.31523	0.00808	0.04529	0.00057	0.01427	0.00023	217	36	278	6	286	4
DQ43 03	33	449	564	0.80	0.32546	0.01028	0.04606	0.00064	0.01646	0.00033	252	47	286	8	290	4
DQ43 04	24	412	424	0.97	0.31845	0.01272	0.04463	0.00072	0.01435	0.00035	274	62	281	10	281	4
DQ43 05	14	165	248	0.66	0.32794	0.01387	0.04698	0.00078	0.01487	0.00044	224	67	288	11	296	5
DQ43 06	16	186	293	0.63	0.32930	0.01245	0.04601	0.00071	0.0145	0.00040	281	58	289	10	290	4
DQ43 07	32	478	593	0.81	0.32167	0.01293	0.04478	0.00073	0.01402	0.00037	290	62	283	10	282	5
DQ43 08	13	156	242	0.64	0.32051	0.01733	0.04490	0.00091	0.01492	0.00058	275	87	282	13	283	6
DQ43 09	25	342	441	0.78	0.32215	0.01527	0.04512	0.00083	0.01549	0.00047	276	75	284	12	284	5
DQ43 10	187	5930	2466	2.40	0.33845	0.00670	0.04524	0.00051	0.01437	0.00015	381	25	296	5	285	3
DQ43 11	7	67	138	0.48	0.30708	0.02223	0.04566	0.00113	0.01396	0.00081	137	117	272	17	288	7
DQ43 12	9	96	182	0.53	0.34661	0.01788	0.04578	0.00089	0.01406	0.00058	409	80	302	13	289	5
DQ43 13	11	134	213	0.63	0.31977	0.01804	0.04475	0.00092	0.01355	0.00056	277	91	282	14	282	6
DQ43 14	21	360	368	0.98	0.31977	0.01329	0.04468	0.00074	0.01467	0.00035	281	65	282	10	282	5
DQ43 15	16	173	295	0.59	0.32260	0.01483	0.04510	0.00080	0.01395	0.00047	280	73	284	11	284	5
DQ43 16	18	222	333	0.67	0.30903	0.01505	0.04527	0.00083	0.01374	0.00047	173	79	273	12	285	5
DQ43 17	42	629	754	0.83	0.32614	0.01064	0.04552	0.00065	0.01398	0.00030	284	49	287	8	287	4
DQ43 18	44	1186	593	2.00	0.28585	0.0217	0.04502	0.00066	0.01333	0.00023		172	255	17	284	4
DQ43 19	22	337	410	0.82	0.32104	0.01501	0.04486	0.00081	0.01377	0.00042	281	74	283	12	283	5
DQ43 20	5	31	98	0.32	0.34280	0.03226	0.04528	0.00147	0.01364	0.00131	409	153	299	24	285	9

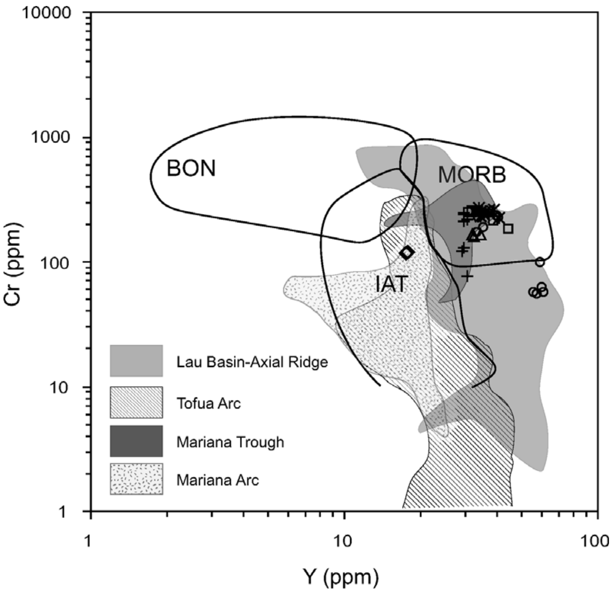

Figure 15. A Cr v. Y discrimination diagram for rocks from the Liuyuan complex, after Pearce *et al.* (1981). BON – boninite, IAT – island arc tholeiite and MORB – mid-oceanic ridge. The fields of the Lau Basin-Axial Ridge, the Tofua Arc, Mariana Trough and Mariana Arc are after Hawkins (2003). Symbols as in Figure 5.

samples plot in the MORB field, including Group 1 and 2 basalts, olivine gabbros and hornblende gabbros, and they overlap with the fields of the Lau Basin Ridge and Mariana Trough. Some Group 3 basalts plot in the MORB field, but all the basalts overlap with the field of the Lau Basin Ridge. The massive gabbros plot in the island arc tholeiite (IAT) field. The Hf/3–Ta–Th diagram (Wood, 1980) is another useful tectonic magmatic discriminant diagram, which can diagnose SSZ settings. The basalt and gabbro samples display a clear SSZ signature (Fig. 16), plotting in the N-MORB and IAT fields, and predominantly on the boundary between N-MORB and IAT compositions. They overlap with basalts from the Lau Basin and the Mariana Trough. All Group 1 basalts plot in the N-MORB field; the Group 2 basalts, olivine gabbros, massive gabbros and hornblende gabbros plot on the margin between IAT and N-MORB and overlap the fields of the Mariana Trough and Lau Basin; the Group 3 basalts mainly plot in the IAT and N-MORB fields; only one sample plots in the E-MORB field. Usually these geochemical relations are interpreted to indicate a back-arc/fore-arc setting. However, in the anatomy of modern island arcs, they define a fore-arc ophiolite (Stern, 2004, 2008, 2009), an interpretation that we favour for the LC in this paper.

All the Liuyuan samples display high positive $\varepsilon_{Nd(t)}$ values (5.7–9.0). Except for the massive gabbros and olivine gabbros, the samples have low $(^{87}Sr/^{86}Sr)_i$ ratios, which are consistent with generation from a mantle-derived magma. Most samples plot immediately to the high $^{87}Sr/^{86}Sr$ side of the mantle array, consistent with mixing of slab-derived subducted components with the mantle source. The high $(^{87}Sr/^{86}Sr)_i$

https://doi.org/10.1017/S0016756811000811 Published online by Cambridge University Press

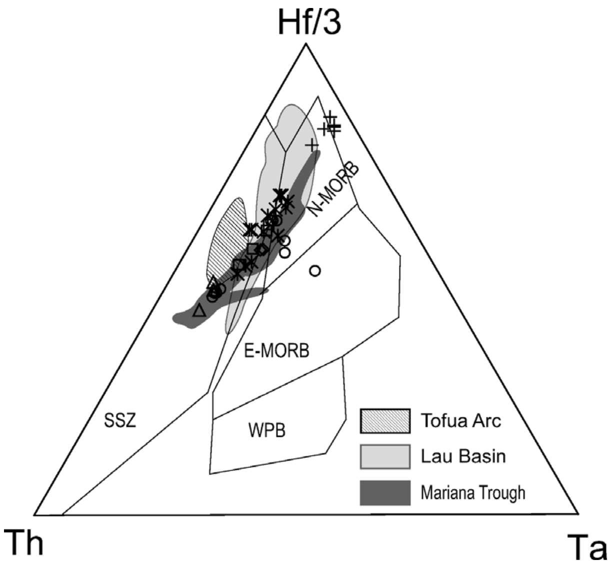

Figure 16. A discrimination diagram for Hf/3–Ta–Th (Wood, 1980; Hawkins, 2003) for rocks of the Liuyuan complex showing fields of N-MORB, E-MORB, WPB (within-plate) and SZZ (supra-subduction zone) magmas. The fields of the Tofua Arc, Lau Basin and Mariana Trough are from Hawkins (2003). Symbols as in Figure 5.

gabbros suggest there has been redistribution of Sr during alteration of the ophiolite. The Sr–Nd isotopes of the basalts vary systematically among the three groups of basalts (Fig. 10; Table 2), with $\varepsilon_{Nd(t)}$ values decreasing from Group 1 to Group 3. We interpret these relations to indicate that the magma was progressively assimilated by island arc crustal components.

In summary, the LC is dominated by MORB-like rocks, which have diagnostic subduction-related geochemical signatures. To explain the full gamut of stratigraphic, structural and geochemical relations, we suggest that the LC formed in a fore-arc (Karsten, Klein & Sherman, 1996; Guivel *et al.* 1999; Saccani & Photiades, 2004). Subsequently, it was accreted to a trench, where it became incorporated into an accretionary prism.

7.b. Age constraints

7.b.1. *Lower limit of age constraints*

As mentioned above, both basalt and gabbro samples in the LC display a clear SSZ signature and are interpreted as a fragment or sliver of a fore-arc. One gabbro has an early Permian age (286 ± 3 Ma). Although it is difficult to obtain the precise age of basalts, regional relationships and isotopic ages can be used to constrain their age.

Based on the regional geology, we propose that the basalts most likely erupted in the period *c.* 286–300 Ma (Zhao *et al.* 2006; Jiang *et al.* 2007). This conclusion is in agreement with the fact that the 286 Ma gabbro was intruded into the basalts (Fig. 4d), which accordingly should post-date them. Therefore, the mafic components of the LC are probably late Carboniferous to early Permian in age.

Considering the fact that all the basalts are thrust-imbricated against fossiliferous Permian limestone and tuffaceous sediments (Zuo *et al.* 1990; Zhao *et al.* 2006; Jiang *et al.* 2007), we propose that the youngest component of the LC is Permian in age. All the late Carboniferous or early Permian ages of the LC can be used to define a lower age limit, which should pre-date the termination of subduction-related accretion of the southernmost Altaids.

The Beishan contains several subducted-related magmatic complexes of Permian age, for example the Hongshishan and Pobei Alaskan-type mafic–ultramafic complexes (Ao *et al.* 2010), the Baishiquan complex with a zircon LA-ICP-MS U–Pb age of 281 ± 0.7 Ma, and the Pobei complex with a zircon SHRIMP U–Pb age of 278 ± 2 Ma (Li *et al.* 2006; Mao *et al.* 2006). Also there are arc-related, Permian granitic intrusions. A granite in the Beidashan area has an $^{40}Ar–^{39}Ar$ age on biotite of 277.0 ± 3.8 Ma, and on hornblende of 275 ± 4 Ma (Lai *et al.* 2007), and the Shanchakou granitic porphyry in the eastern Tianshan has a zircon SHRIMP age of 278 ± 4 Ma (Li *et al.* 2004).

7.b.2. *Upper limit of age constraints*

Published isotopic ages combined with regional tectonostratigraphic data can place an upper limit on the time of final accretion in the Beishan. Several syn-collisional and post-collisional intrusions are early Permian or later. For example, the Weiya syn-collisional granitic complex has a zircon SHRIMP U–Pb age range from 233 to 246 Ma (Zhang *et al.* 2005), the syn-collisional, a rare metal pegmatite deposit at Jingerquan has an $^{40}Ar–^{39}Ar$ early Triassic age of 243 ± 2 Ma on mica (Chen *et al.* 2006), and post-collisional lamprophyre intrusions in the Liuyuan area have $^{40}Ar–^{39}Ar$ plateau ages of 218.7 ± 1.4 Ma and 220.6 ± 1.5 Ma on phlogopite (Liu, Zhao & Guo, 2006). Accordingly, the termination of orogenesis in the Beishan orogen should have been in early Triassic time. Finally, the Huaniushan and Huitongshan granites that have $^{40}Ar–^{39}Ar$ ages of 192 ± 2 Ma and 194 ± 1 Ma on potassium feldspar, respectively, were intruded in post-collisional times (Nie *et al.* 2002*b*; Jiang *et al.* 2003).

In the SW Tianshan, subduction took place after late Permian time. For example, subduction gave rise to eclogites that have zircon SHRIMP U–Pb metamorphic ages ranging from 230 Ma to 225 Ma (Zhang *et al.* 2007).

In late Permian and Triassic time, regional compression was extensive in the Beishan and adjacent areas. For example, Zheng *et al.* (1996) demonstrated that major thrusts developed in the Jurassic. Further west, mylonites in a thrust zone in the eastern Tianshan have an $^{40}Ar–^{39}Ar$ age of 167–247 Ma on mica (Cunningham *et al.* 2003), and sericite in a thrust mylonite zone has an $^{40}Ar–^{39}Ar$ plateau age of 243.8 ± 1.8 Ma (Wang *et al.* 2008).

7.c. Tectonic model

In early Permian time, the Liuyuan ocean, one branch of the Palaeo-Asian ocean, was being subducted to give rise to the active margin of the Huaniushan arc. To explain the relevant times of intrusion of syn-collisional and post-collisional magmatic rocks, we suggest that, when the ocean was closing, a mid-oceanic ridge was subducted below the trench on the southern margin of the Huaniushan arc; this is indicated by MORB and subduction-related geochemistry combined with field relationships. Our suggested evolution is illustrated in Figure 17.

The ridge subduction created a slab window, which induced a lateral flow of fertile material from the mantle wedge into the MORB-type mantle, resulting in mixing and formation of heterogeneous mantle. The coupling of mantle upwelling might have interacted with the subduction-related magma/fluid efflux from the subduction devolatilization, which in turn permitted formation of the Group 1 and 2 basalts and gabbros; the Group 3 basalts with an OIB-type geochemical signature developed through the slab window. A comparable tectonic scenario took place at the Chile Ridge in the Chile triple junction, and at the East Pacific Rise in the Mexico triple junction (Karsten, Klein & Sherman, 1996; Guivel *et al*. 1999; Saccani & Photiades, 2004).

In the slab window zone, asthenospheric material infiltrated the mantle wedge and induced the generation of mantle-derived magmas (Guivel *et al*. 1999; Ferrari, Petrone & Francalanci, 2001). The mid-ocean ridge subduction also led to formation of strike-slip faults in the supra-subduction region. The mantle-derived magma rose up and along the strike-slip fault channels and intruded or erupted. In consequence, widespread basalts and Alaskan-type complexes developed along these large strike-slip faults in the eastern Tianshan and Beishan, such as the Pobei complex in the Beishan (Ao *et al*. 2010), and the Huangshan and Baishiquan complexes in the eastern Tianshan (Xiao *et al*. 2004*b*; Mao *et al*. 2006). Extensive basalts erupted in the back-arc region of the Hongliuhe and Santanghu areas have OIB and E-MORB geochemical signatures (Zhao *et al*. 2006; Pan *et al*. 2008), and Permian laser isochron $^{40}Ar–^{39}Ar$ ages of 278 ± 17 Ma and 305 ± 14 Ma (Pan *et al*. 2008).

In the following subduction-accretionary history, the LC was accreted onto a fore-arc. When the Liuyuan ocean closed, the LC was thrust as an imbricated ophiolitic stack between the Huaniushan and Shibanshan arcs. This sequence of events is well established in the evolution of many accretionary orogens (Cluzel, Aitchison & Picard, 2001; Stern, 2004, 2008, 2009; Ueda & Miyashita, 2005).

7.d. Tectonic implications

The final closure time of the Palaeo-Asian ocean, and the time of formation of the terminal suture zone of the Altaids are subjects of current hot debate. The LC in the Beishan orogenic collage provides key evidence to address this controversy.

The main part of the LC has MORB geochemical signatures displaying high positive $\varepsilon_{Nd(t)}$ values (5.8–9.0) and low initial Sr ratios, and some OIB characteristics (Group 3 basalts), and yet some rocks exhibit subduction-related signatures such as depletion in Nb–Ta and Ti. Accordingly, we interpret the evolution of the LC as follows: MORB oceanic crust was created in a mid-oceanic ridge near a trench in early Permian time. It formed where fluids released from melted sediments from a deep subducting slab were injected into the ocean floor-ophiolitic magmas in a supra-subduction setting. The fore-arc was probably narrow, enabling volcaniclastic tuffs and fragments from a nearby arc volcano to be deposited on the cherts and basalts. Our new data demonstrate for the first time that the Palaeo-Asian ocean in the Beishan orogenic collage in the middle of the Southern Tien Shan-Solonker suture zone did not close until late Permian time or later.

Our results from the LC are consistent with and support well-documented floral, faunal and palaeomagnetic data. Faunal and floral data indicate that the Tarim plate collided with Palaeo-Asia in late Permian time. For example, Sun (1973) and Qu *et al*. (2002) reported late Permian–Triassic dicynodonts in the Turfan Basin, a group of reptiles that came from the Gondwana continent. Palaeobotanical data indicate that Angaran flora migrated into the Tarim in late Permian time, where the previous dominant flora were Pangaean of early Permian age (Ou *et al*. 1993, 2004; Wu, 1993; Fang, 1997; Zhu, 1997, 2001; Guo, 2001; Li, Sun & Zheng, 2002). The above authors documented a detailed history as follows: in early Permian time, Pangaean flora were still predominant in the Tarim plate; in middle Permian time, Angaran flora began to migrate into the Tarim plate forming a mixed floral species; from late middle Permian to late Permian time, the Tarim plate became dominated by Angaran flora. These relations indicate that close proximity and initial contiguity of the two plates began in middle Permian time, that collision between the two plates started by late Permian time, and the timing of these events is consistent with palaeomagnetic data (Li, Sun & Zheng, 2002).

However, the final amalgamation was more complicated in late Permian to mid-Triassic time than we previously recognized (Xiao, Kröner & Windley, 2009; Xiao *et al*. 2010*a*). Multiple linear components were probably amalgamated in a complex manner with oblique, orthogonal and parallel interactions (Xiao, Kröner & Windley, 2009; Xiao *et al*. 2010*a,b*). Large-scale oroclinal bending, rotation and strike-slip faulting occurred simultaneously or mutually overlapped. This gave rise to a complex tectonic scenario in which the final amalgamation time varied considerably along strike of the major suture zone of the southern Altaids (Xiao *et al*. 2009, 2010*a,b*). The terminal stages of the accretionary orogeny took place in late Permian to

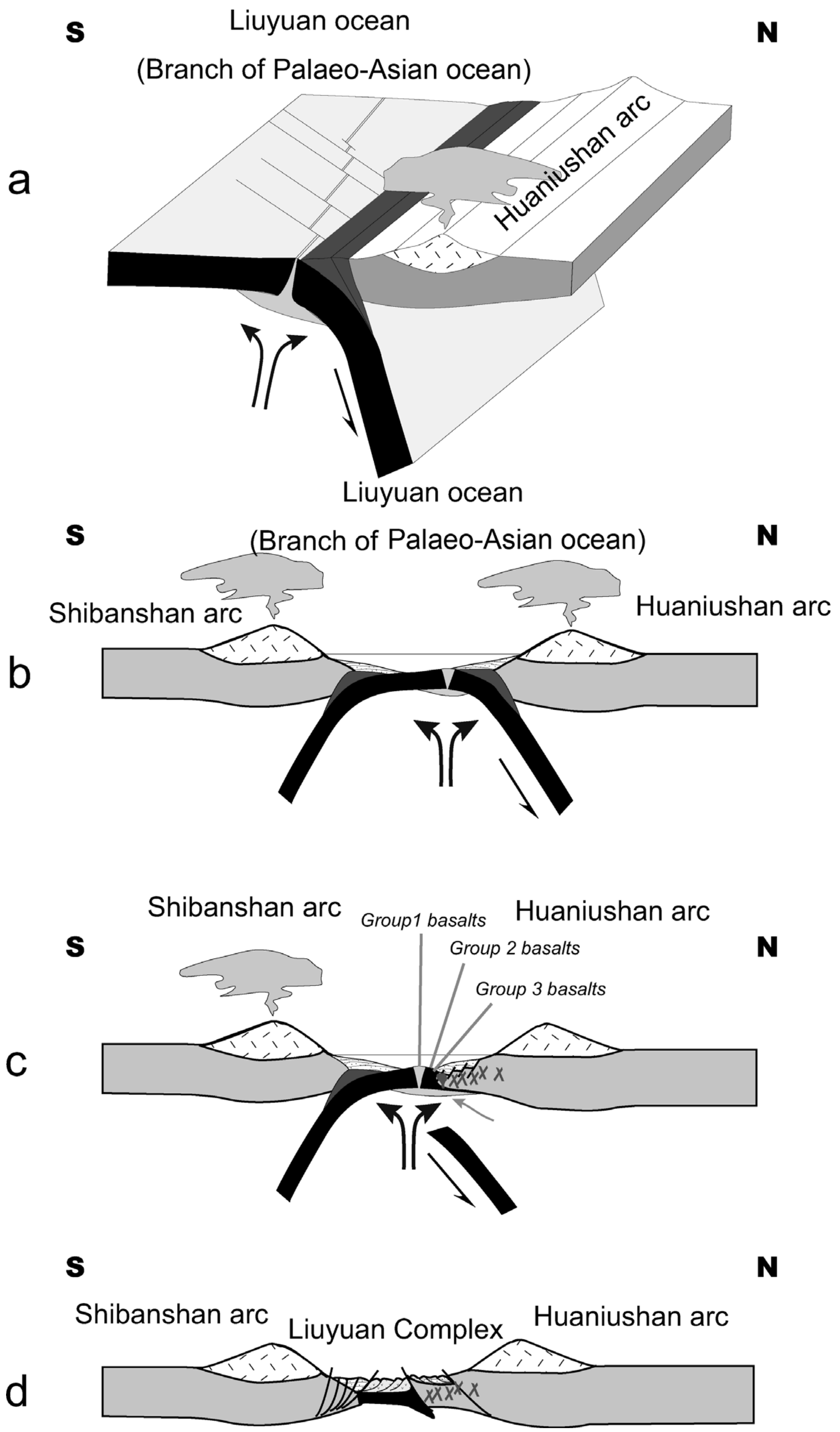

Figure 17. A three-dimensional tectonic model to explain the evolution of the Liuyuan complex from late Carboniferous to Permian time. (a) In the late Carboniferous to early Permian, a fore-arc was constructed by subduction of a spreading ridge of the Liuyuan ocean, a branch of the Palaeo-Asian ocean, beneath the Huaniushan arc to the south. (b) The Liuyuan ocean was subducted possibly both to the south and the north, giving rise to the Shibanshan arc and late phases of the Huaniushan arc, respectively. (c) Group 1, 2 and 3 basalts were generated in the fore-arc of the Huaniushan arc. (d) Final amalgamation of the Shibanshan and Huaniushan arcs possibly in late Permian time formed the Liuyuan ophiolitic complex.

https://doi.org/10.1017/S0016756811000811 Published online by Cambridge University Press

middle Triassic time (Xiao, Kröner & Windley, 2009; Xiao *et al*. 2009, 2010*a,b*).

Acknowledgements. This paper is part of the first author's Ph.D. thesis supervised by WJX. We thank Jiliang Li, Shoufa Lin, Yong Yong, Ji'en Zhang, Nathan Cleven and Dongfang Song for collaboration in the field. Guochao Zuo and Xueyi Xu are acknowledged for discussions on the tectonics of the Beishan. We appreciate the constructive comments of Sanzhong Li, an anonymous referee and the editor, Phil Leat. This study was financially supported by funds from the Chinese State 973 Project (2007CB411307), the Innovative Program of the Chinese Academy of Sciences (KZCX2-YW-Q04-08), Chinese State 305 Projects (2011BAB06B04-1, 2011BAB06B04-3) and the NSFC Projects (40725009, 40523003, 40973036). This paper is a contribution to the International Lithosphere Programs (ERAS and Topo-Central-Asia).

References

AO, S. J., XIAO, W. J., HAN, C. M., MAO, Q. G. & ZHANG, J. E. 2010. Geochronology and geochemistry of Early Permian mafic-ultramafic complexes in the Beishan area, Xinjiang, NW China: implications for late Paleozoic tectonic evolution of the southern Altaids.*Gondwana Research* **18**, 466–78.

BAZHENOV, M. L., COLLINS, A. Q., DEGTYAREV, K. E., LAVASHOVA, N. M., MIKOLAICHUK, A. V., PAVLOV, V. E. & VAN DER VOO, R. 2003. Paleozoic northward drift of the North Tien Shan (Central Asia) as revealed by Ordovician and Carboniferous paleomagnetism. *Tectonophysics* **366**, 113–41.

BEDARD, J. 1999. Petrogenesis of boninites from the Betts Cove ophiolite, Newfoundland, Canada: identification of subducted source components. *Journal of Petrology* **40**, 1853–89.

BOYNTON, W. V. 1984. Geochemistry of the rare earth elements: meteorite study. In *Rare Earth Element Geochemistry* (ed. P. Henderson), pp. 63–114. Amsterdam: Elsevier.

BUCHAN, C., PFÄNDER, J., KRÖNER, A., BREWER, T. S., TOMURTOGOO, O., TOMURHUU, D., CUNNINGHAM, D. & WINDLEY, B. F. 2002. Timing of accretion and collisional deformation in the Central Asian orogenic belt: implications of granite geochronology in the Bayankhongor ophiolite zone. *Chemical Geology* **192**, 23–45.

CHEN, F., HAGNER, E. & TODT, W. 2000. Zircon ages. Nd isotopic and chemical compositions of orthogneisses from the Black Forest, Germany – evidence for a Cambrian magmatic arc. *International Journal of Earth Sciences* **88**, 791–802.

CHEN, Z. H., WANG, D. H., GONG, Y. F., CHEN, Y. C. & CHEN, S. P. 2006. ^{40}Ar-^{39}Ar isotope dating of muscovite from Jingerquan pegmatite rare metal deposit in Hmni, Xinjiang, and its geological significance. *Mineral Deposits* **25**, 470–6 (in Chinese with English abstract).

CLUZEL, D., AITCHISON, J. C. & PICARD, C. 2001. Tectonic accretion and underplating of mafic terranes in the late Eocene intraoceanic fore-arc of New Caledonia (Southwest Pacific); geodynamic implications. *Tectonophysics* **340**, 23–59.

COLEMAN, R. 1989. Continental growth of Northwest China. *Tectonics* **8**, 621–35.

CUNNINGHAM, D., OWEN, L. A., SNEE, L. W. & LI, J. L. 2003. Structural framework of a major intracontinental orogenic termination zone: the easternmost Tien Shan, China. *Journal of the Geological Society, London* **160**, 575–90.

DILEK, Y. & FURNES, H. 2011. Ophiolite genesis and global tectonics: geochemical and tectonic fingerprinting of ancient oceanic lithosphere. *Geological Society of America Bulletin* **123**, 387–411.

DOBRETSOV, N. L., BERZIN, N. A. & BUSLOV, M. M. 1995. Opening and the tectonic evolution of Paleo-Asian ocean. *International Geology Review* **35**, 335–60.

FANG, Z. J. 1997. Southward intrusion of Angaran migrants into Tarim during the latest Permian and the global climatic cooling event. *Acta Geoscientica Sinica* **36**, 65–76 (in Chinese with English abstract).

FERRARI, L., PETRONE, C. M. & FRANCALANCI, L. 2001. Generation of oceanic-island basalt-type volcanism in the western Trans-Mexican volcanic belt by slab rollback, asthenosphere infiltration, and variable flux melting. *Geology* **29**, 507–10.

GAO, J., LI, M., XIAO, X., TANG, Y. & HE, G. 1998. Paleozoic tectonic evolution of the Tianshan orogen, northwestern China. *Tectonophysics* **287**, 213–31.

GSBGMR 1989. *Regional Geology of Gansu Province, Geological Memoirs*. Beijing: Geological Publishing House.

GUIVEL, C., LAGABRIELLE, Y., BOURGOIS, J., MAURY, R. C., FOURCADE, S. & MARTIN, H. 1999. New geochemical constraints for the origin of ridge-subduction-related plutonic and volcanic suites from the Chile Triple Junction (Taitao peninsula and Site 863, Leg ODP 141 on the Tqitao Ridge). *Tectonophysics* **311**, 83–111.

GUO, F. X. 2001. Paleozoic tectono-paleobiogeography of Xinjiang, China. *Xinjiang Geology* **19**, 20–6.

HAN, B., WANG, S., JAHN, B.-M., HONG, D., KAGAMI, H. & SUN, Y. 1997. Depleted mantle source for the Ulungur River A-type granites from North Xinjiang, China: geochemistry and Nd-Sr isotopic evidence, and implications for the Phanerozoic crustal growth. *Chemical Geology* **138**, 135–59.

HAWKINS, J. W. 1994. Petrologic synthesis: Lau Basin transect (Leg 135). In *Proceedings of the Ocean Drilling Program, Scientific Results, vol. 135* (eds J. Hawkins, L. Parson, J. Allan, *et al.*), pp. 879–905. College Station, Texas.

HAWKINS, J. W. 2003. Geology of supra-subduction zones-Implications for the origin of ophiolites. In *Ophiolite Concept and the Evolution of Geological Thought* (eds Y. Dilek & S. Newcomb), pp. 227–68. Geological Society of America, Special Papers no. 373.

HENDRIX, M. S., GRAHAM, S. A., AMORY, J. Y. & BADARCH, G. 1996. Noyon Uul Syncline, southern Mongolia; Lower Mesozoic sedimentary record of the tectonic amalgamation of Central Asia. *Geological Society of America Bulletin* **108**, 1256–74.

HENDRIX, M. S. 2000. Evolution of Mesozoic sandstone composition, southern Junggar, northern Tarim, and western Turpan basins, Northwest China: a detrital record of the ancestral Tian Shan. *Journal of Sedimentary Research* **70**, 520–32.

HOECK, V., KOLLER, F., MEISEL, T. & ONUZI, K. 2002. The Jurassic South Albanian ophiolites: MOR- vs. SSZ-type ophiolites. *Lithos* **65**, 143–64.

JIANG, S. H., NIE, F. J., CHEN, W., LIU, Y., BAI, D. M., LIU, X. Y. & ZHANG, S. H. 2003. Discovery of Yanshanian K-feldspar granite in Huitongshan Copper Deposit, Gansu Province, and its implication. *Mineral Deposits* **22**, 185–90.

JIANG, C. Y., XIA, M. Z., YU, X., DAI, D. X., WEI, W. & YE, S. F. 2007. Liuyuan trachybasalt belt in the northeastern Tarim Plate: products of asthenosphere mantle decompressional melting. *Acta Petrologica Sinica* **23**, 1765–78 (in Chinese with English abstract).

KARSTEN, J. L., KLEIN, E. M. & SHERMAN, S. B. 1996. Subduction zone geochemical characteristics in ocean ridge basalts from the southern Chile Ridge: implications of modem ridge subduction systems for the Archean. *Lithos* **37**, 143–61.

LAI, X. R., JIANG, S. H., QIU, X. P., LIU, Y., HU, P. & ZHANG, W. Y. 2007. ^{40}Ar-^{39}Ar age and geochemical features of Hercynian intermediate acidic rock in Beidashan Rock Belt, Aixa. *Acta Geologica Sinica* **81**, 370–80.

LAMB, M. A. & BADARCH, G. 2000. Paleozoic sedimentary basins and volcanic-arc systems of southern Mongolia; new stratigraphic and sedimentologic constraints. In *Tectonic Studies of Asia and the Pacific Rim: A tribute to Benjamin M. Page (1911–1997)* (eds W. G. Ernst & R. G. Coleman), pp. 107–41. Columbia, MD, United States: Bellweather Publishing for the Geological Society of America.

LAMB, M. A., BADARCH, G., NAVRATIL, T. & POIER, R. 2008. Structural and geochronologic data from the Shin Jinst area, eastern Gobi Altai, Mongolia: implications for Phanerozoic intracontinental deformation in Asia. *Tectonophysics* **451**, 312–30.

LI, H. Q., CHEN, F. W., LU, Y. F., YANG, H. M., GUO, J. & MEI, Y. P. 2004. Zircon SHRIMP U-Pb age and strontium isotopes of mineralized granitoid in the Sanchakou copper polymetallic deposit, East Tianshan Mountains. *Acta Geoscientica Sinica* **25**, 191–5 (in Chinese with English abstract).

LI, H. Q., CHEN, F. W., MEI, Y. P., WU, H., CHEN, S. L., YANG, J. Q. & DAI, Y. C. 2006. Isotopic ages of No. 1 intrusive body in Pobei mafic-ultramafic belt of Xinjiang and their geological significance. *Mineral Deposits* **25**, 463–9.

LI, Y. A., SUN, D. J. & ZHENG, J. 2002. Paleomagnetic study tectonic evolution of Xinjiang and its neighboring regions. *Xinjiang Geology* **20**, 193–235 (in Chinese with English abstract).

LIU, C., ZHAO, Z. H. & GUO, Z. J. 2006. Chronology and geochemistry of lamprophyre dykes from Beishan area, Gansu Province and implications for the crust-mantle interaction. *Acta Petrologica Sinica* **25**, 194–1306 (in Chinese with English abstract).

LIU, X. C., CHEN, B. L., JAHN, B. M., WU, G. G. & LIU, Y. S. 2011. Early Paleozoic (ca. 465 Ma) eclogites from Beishan (NW China) and their bearing on the early evolution of the southern Central Asian Orogenic Belt. *Journal of Asian Earth Sciences* **42**, 715–31.

LIU, X. Y. & WANG, Q. 1995. Tectonics of orogenic belts in the Beishan Mountains, western China and their evolution. *Geoscience Studies* **28**, 37–48 (in Chinese with English abstract).

MA, R. S., SHU, L. S. & SUN, J. 1997. *Tectonic Evolution and Metalogeny of Eastern Tianshan Mountains*. Beijing: Geological Publishing House.

MAO, Q. G., XIAO, W. J., HAN, C. M., YUAN, C. & SUN, M. 2008. Late paleozoic southward accretionary polarity of the eastern Junggar orogenic belt: insight from the Dajiashan and other A-type granites. *Acta Petrologica Sinica* **24**, 733–42.

MAO, Q. G., XIAO, W. J., HAN, C. M., SUN, M., YUAN, C., YAN, Z., LI, J. L., YONG, Y. & ZHANG, J. E. 2006. Zircon U-Pb age and the geochemistry of the Baishiquan mafic-ultramafic complex in the eastern Tianshan, Xinjiang: constraints on the closure of the Paleo-Asian Ocean. *Acta Petrologica Sinica* **22**, 153–62 (in Chinese with English abstract).

MAO, Q. G., XIAO, W. J., HAN, C. M., SUN, M., YUAN, C., ZHANG, J., AO, S. J. & LI, J. L. 2010. Discovery of Middle-Silurian adakite granite and its tectonic significance in Liuyuan area, Beishan Mountains, NW China. *Acta Petrologica Sinica* **26**, 584–96 (in Chinese with English abstract).

MEI, H. L., LI, H. M., LU, S. N., YU, H. F., ZUO, Y. C. & LI, Q. 1999. The age and origin of the Liuyuan granitoid, northwestern Gansu. *Acta Petrologica et Mineralogica* **18**, 14–17 (in Chinese with English abstract).

MEI, H., YU, H., LI, Q., LU, S., LI, H., ZUO, Y., ZUO, G., YE, D. & LIU, J. 1998. The first discovery of eclogite and Palaeoproterozoic granitoids in the Beishan area, northwestern Gansu Province, China. *Chinese Science Bulletin* **44**(4), 356–61.

NEAL, C. R., MAHONEY, J. J. & CHAZEY III, W. J. 2002. Mantle sources and the highly variable role of continental lithosphere in basalt petrogenesis of the Kerguelen plateau and Broken ridge LIP: results from ODP Leg 183. *Journal of Petrology* **37**, 1177–205.

NIE, F. J., JIANG, S. H., BAI, D. M., WANG, X. L., SU, X. X., LI, J. C., LIU, Y. & ZHAO, X. M. 2002*a*. *Metallogenic Studies and Ore Prospecting in the Conjunction Area of Inner Mongolia Autonomous Region, Gansu Province and Xinjiang Uygur Autonomous Region (Beishan Mt.), Northwest China*. Beijing: Geological Publishing House.

NIE, F. J., JIANG, S. H., LIU, Y., CHEN, W., LIU, X. Y. & ZHANG, S. H. 2002*b*. 40Ar/39Ar isotopic age dating on K-feldspar separates from eastern Huanniushan granite, Gansu province, and its geological significance. *Chinese Journal of Geology* **37**, 415–22.

OU, Y. S., WANG, Z., ZHAN, J. Z. & ZHOU, Y. X. 1993. A preliminary discussion on phytoprovincial characters of Carboniferous-Permian palynofloras in Xinjiang, NW China. *Acta Micropalaeontologica Sinica* **10**, 237–55 (in Chinese with English abstract).

OU, Y. S., ZHU, H. C., ZHAN, J. Z. & WANG, Z. 2004. Comparison of Permian palynofloras from the Junggar and Tarim basins and its bearing on phytoprovincialism and stratigraphy. *Journal of Stratigraphy* **28**, 193–207 (in Chinese with English abstract).

PAN, J. H., GUO, Z. J., LIU, C. & ZHAO, Z. H. 2008. Geochronology, geochemistry and tectonic implications of Permian basalts in Hongliuhe area on the border between Xinjiang and Gansu. *Acta Petrologica Sinica* **24**, 793–802.

PEARCE, J. A., ALABASTER, T., SHELTON, A. W. & SEARLE, M. P. 1981. The Oman ophiolite as a Cretaceous arc-basin complex: evidence and implications. *Philosophical Transactions of the Royal Society of London, Series A* **300**, 299–317.

QU, J. F., XIAO, W. J., WINDLEY, B. F., HAN, C. M., MAO, Q. G., AO, S. J. & ZHANG, J. E. 2011. Ordovician eclogites from the Chinese Beishan: implications for the tectonic evolution of the southern Altaids. *Journal of Metamorphic Geology* **29**, 803–20. First published online 26 April 2011. doi:10.1111/j.1525-1314.2011.00942.x.

QU, X., WU, S. Z., LI, Y. A. & LI, Q. 2002. Dicynodont and ecological environment of late Permian to early stage of middle Triassic at Junggar southern margin-Turpan. *Xinjiang Geology* **20**, 187–91 (in Chinese with English abstract).

SACCANI, E. & PHOTIADES, A. 2004. Mid-ocean ridge and supra-subduction affinities in the Pindos ophiolites (Greece): implications for magma genesis in a forearc setting. *Lithos* **73**, 229–53.

ŞENGÖR, A. M. C. & NATAL'IN, B. 1996. Turkic-type orogeny and its role in the making of the continental crust. *Annual Reviews of Earth and Planetary Sciences* **24**, 263–337.

ŞENGÖR, A. M. C., NATAL'IN, B. A. & BURTMAN, U. S. 1993. Evolution of the Altaid tectonic collage and Paleozoic crustal growth in Eurasia. *Nature* **364**, 209–304.

SHERVAIS, J. W. 1982. Ti-V plots and the petrogenesis of modern and ophiolitic lavas. *Earth and Planetary Science Letters* **59**, 101–18.

SHI, Y. S., LU, H. F., JIA, D., CAI, D. S., WU, S. M. & CHEN, C. M. 1994. Paleozoic plate-tectonic evolution of the Tarim and western Tianshan regions, western China. *International Geology Reviews* **36**, 1058–66.

STERN, R. J. 2004. Subduction initiation: spontaneous and induced. *Earth and Planetary Science Letters* **226**, 275–92.

STERN, R. J. 2008. Neoproterozoic crustal growth: the solid Earth system during a critical episode of Earth history. *Gondwana Research* **14**, 33–50.

STERN, R. J. 2009. The anatomy and ontogeny of modern intra-oceanic arc systems. In *The Evolving Continents: Understanding Processes of Continental Growth* (eds T. M. Kusky, M. G. Zhai & W. J. Xiao), pp. 7–34. Geological Society of London, Special Publication no. 338.

SUN, A. L. 1973. Permo-Triassic dicynodonts from Tufan, Sinkiang. In *Permo-Triassic Vertebrate Fossils of the Turfan Basin*, pp. 53–68. Memoir IVPP Academia Sinica.

SUN, S. S. & MCDONOUGH, W. F. 1989. Chemical and isotopic systematic of oceanic basalts: implications for mantle composition and process. In *Magmatism in the Ocean Basins* (eds A. D. Saunders & M. J. Norry), pp. 313–45. Geological Society of London, Special Publication no. 42.

TEJADA, M. L., MAHONEY, J. J., DUNCAN, R. A. & HAWKINS, M. P. 1996. Age and geochemistry of basement and alkalic rocks of Malaita and Santa Isabel, Solomon island, southern margin of Ontong Java Plateau. *Journal of Petrology* **37**, 361–94.

TIAN, Y. Z. 1993. Studies the characteristic and characteristic of contain gold about the Shijinpo intrusion in Beishan Mountains, Gansu Province. *Geology School of Xi'an* **15**, 62–8 (in Chinese with English abstract).

UEDA, H. & MIYASHITA, S. 2005. Tectonic accretion of a subducted intraoceanic remnant arc in Cretaceous Hokkaido, Japan, and implications for evolution of the Pacific northwest. *Island Arc* **14**, 582–98.

WANG, Q. L., CHEN, W., HAN, D., WANG, C. Y., LIU, X. Y. & ZHANG, H. 2008. The age and mechanism of formation of the Jinwozi gold deposit, Xinjiang. *Geology in China* **35**, 286–92.

WINCHESTER, J. A. & FLOYD, P. A. 1977. Geochemical discrimination of different magma series and their differentiation products using immobile elements. *Chemical Geology* **20**, 325–43.

WINDLEY, B. F., ALEXEIEV, D., XIAO, W., KRÖNER, A. & BADARCH, G. 2007. Tectonic models for accretion of the Central Asian Orogenic belt. *Journal of the Geological Society, London* **164**, 31–47.

WOOD, D. A. 1980. The application of a Th-Hf-Ta diagram to problems of tectonomagmatic classification and to establishing the nature of crustal contamination of basaltic lavas of the British Tertiary volcanic province. *Earth and Planetary Science Letters* **50**, 11–30.

WU, F. Y., YANG, Y. H., XIE, L. W., YANG, J. H. & XU, P. 2006. Hf isotopic compositions of the standard zircons and baddeleyites used in U-Pb geochronology. *Chemical Geology* **234**, 105–26.

WU, S. Z. 1993. Intrusion of exotic plants of late Permian into the northern margin of Tarim. *Xinjiang Geology* **11**, 140–6 (in Chinese with English abstract).

XBGMR 1993. *Regional Geology of Xinjiang Autonomous Region, Geological Memoirs, Ser. 1, No. 32, Map Scale 1: 1,500,000*. Beijing: Geological Publishing House.

XIAO, W. J., HAN, C. M., YUAN, C., SUN, M., LIN, S. F., CHEN, H. L., LI, Z. L., LI, J. L. & SUN, S. 2008. Middle Cambrian to Permian subduction-related accretionary orogenesis of North Xinjiang, NW China: implications for the tectonic evolution of Central Asia. *Journal of Asian Earth Sciences* **32**, 102–17.

XIAO, W. J., HUANG, B. C., HAN, C. M., SUN, S. & LI, J. L. 2010*a*. A review of the western part of the Altaids: a key to understanding the architecture of accretionary orogens. *Gondwana Research* **18**, 253–73.

XIAO, W. J., KRÖNER, A. & WINDLEY, B. F. 2009. Geodynamic evolution of Central Asia in the Paleozoic and Mesozoic. *International Journal of Earth Sciences* **98**, 1185–8.

XIAO, W. J., WINDLEY, B. F., BADARCH, G., SUN, S., LI, J. L., QIN, K. Z. & WANG, Z. H. 2004*a*. Palaeozoic accretionary and convergent tectonics of the southern Altaids: implications for the lateral growth of Central Asia. *Journal of the Geological Society, London* **161**, 339–42.

XIAO, W. J., WINDLEY, B. F., HAO, J. & ZHAI, M. G. 2003. Accretion leading to collision and the Permian Solonker suture, Inner Mongolia, China: termination of the Central Asian orogenic belt. *Tectonics* **22**, 1069, doi: 10.1029/2002TC1484.

XIAO, W. J., WINDLEY, B. F., HUANG, B. C., HAN, C. M., YUAN, C., CHEN, H. L., SUN, M., SUN, S. & LI, J. L. 2009. End-Permian to mid-Triassic termination of the accretionary processes of the southern Altaids: implications for the geodynamic evolution, Phanerozoic continental growth, and metallogeny of Central Asia. *International Journal of Earth Sciences* **98**, 1189–287.

XIAO, W. J., ZHANG, L. C., QIN, K. Z., SUN, S. & LI, J. L. 2004*b*. Paleozoic accretionary and collisional tectonics of the Eastern Tianshan (China): implications for the continental growth of central Asia. *American Journal of Science* **304**, 370–95.

XIAO, W. J., MAO, Q. G., WINDLEY, B. F., HAN, C. M., QU, J. F., ZHANG, J. E., AO, S. J., GUO, Q. Q., CLEVEN, N. R., LIN, S. F., SHAN, Y. H. & LI, J. L. 2010*b*. Paleozoic multiple accretionary and collisional processes of the Beishan orogenic collage. *American Journal of Science* **310**, 1553–94.

XU, P., WU, F. Y., XIE, L. W. & YANG, Y. H. 2004. Hf isotopic compositions of the standard zircons for U-Pb dating. *Chinese Science Bulletin* **49**, 1643–8.

YANG, J. S., WU, C. L., CHEN, S. Y., SHI, R. D., ZHANG, J. X., MENG, F. C., ZUO, G. C., WU, H. Q. & CONSTANTINOVSKAYA, E. 2006. Neoproterozoic eclogitic metamorphic age of the Beishan eclogite of Gansu, China: evidence from SHRIMP U-Pb isotope dating. *Geology in China* **33**, 317–25.

YU, H. F., LU, S. N., MEI, H. L., ZHAO, C. F., LI, H. S. & LI, H. M. 1999. Characteristics of Neoproterozoic eclogite-granite zones and deep level ductile shear zone in western China and their significance for continental reconstruction. *Acta Petrologica Sinica* **15**, 532–8.

YUAN, H. L., WU, F. Y., GAO, S., LIU, X. M., MA, Z. P. & WANG, L. S. 2003. LA-ICP-MS zircon U-Pb dating and REE analysis of the Cenozoic intrusion in northeast China. *Chinese Science Bulletin* **48**, 1511–20 (in Chinese).

ZHANG, L. F., AI, Y. L., LI, X. P., RUBATTO, D., SONG, B., WILLIAMS, S., SONG, S. G., ELLIS, D. & LIOU, J. G. 2007. Triassic collision of western Tianshan orogenic belt, China: evidence from SHRIMP U–Pb dating of zircon from HP/UHP eclogitic rocks. *Lithos* **96**, 266–80.

ZHANG, Z. Z., GU, L. X., WU, H., XI, A. H. & TANG, J. H. 2005. Zircons SHRIMP dating of the Weiya intrusion eastern Tianshan Mountains and its geological significance. *Acta Geologica Sinica* **12**, 472–7.

ZHAO, Z. H., GUO, Z. J., HAN, B. F., WANG, Y. & LIU, C. 2006. Comparative study on Permian basalts from eastern Xinjiang-Beishan area of Gansu province and its tectonic implications. *Acta Petrologica Sinica* **22**, 1279–93 (in Chinese with English abstract).

ZHAO, Z. H., GUO, Z. J. & WANG, Y. 2007. Geochronology, geochemical characteristics and tectonic implications of the granitoids from Liuyuan area, Beishan, Gansu province, northwest China. *Acta Petrologica Sinica* **23**, 1847–60 (in Chinese with English abstract).

ZHENG, Y., ZHANG, Q., WANG, Y., LIU, R., WANG, S. G., ZUO, G., WANG, S. Z., LKAASUREN, B., BADARCH, G. & BADAMGARAV, Z. 1996. Great Jurassic thrust sheets in Beishan (North Mountains); Gobi areas of China and southern Mongolia. *Journal of Structural Geology* **18**(9), 1111–26.

ZHOU, M.-F., LESHER, C. M., YANG, Z. X., LI, J. W. & SUN, M. 2004. Geochemistry and petrogenesis of 270 Ma Ni-Cu-(PGE) sulfide-bearing mafic intrusions in the Huangshan district, Eastern Xinjiang, Northwest China: implications for the tectonic evolution of the Central Asian orogenic belt. *Chemical Geology* **209**, 233–57.

ZHOU, X. H., SUN, M., ZHANG, G. H. & CHEN, S. H. 2002. Continental crust and lithospheric mantle interaction beneath North China: isotopic evidence from granulite xenoliths in Hannuoba, Sino-Korean craton. *Lithos* **62**, 111–24.

ZHU, H. C. 1997. Discussion on phytoprovincial characters of Permian palynofloras from Tarim Basin and their implications on the evolution of Tarim block. *Acta Micropalaeontologica Sinica* **14**, 315–20 (in Chinese with English abstract).

ZHU, H. C. 2001. The floral response to the Permian tectonic evolution in Tarim plate. *Acta Geoscientica Sinica* **22**, 67–72 (in Chinese with English abstract).

ZINDLER, A. & HART, S. R. 1986. Chemical geodynamics. *Annual Reviews of Earth and Planetary Sciences* **14**, 493–571.

ZUO, G. C., LIU, Y. K. & LIU, C. Y. 2003. Framework and evolution of the tectonic structure in Beishan area across Gansu Province, Xinjiang Autonomous region and Inner Mongolia Autonomous Region. *Acta Geologica Gansu* **12**, 1–15 (in Chinese with English abstract)

ZUO, G., ZHANG, S., HE, G. & ZHANG, Y. 1991. Plate tectonic characteristics during the early Paleozoic in Beishan near the Sino-Mongolian border region, China. *Tectonophysics* **188**(3–4), 385–92.

ZUO, G. C., ZHANG, S. L., WANG, X., JIN, S. Q., HE, G. Q., ZHANG, Y., LI, H. C. & BAI, W. C. 1990. *Plate Tectonics and Metallogenic Regularities in Beishan region*. Peking University Publishing House.

Appendix 1. Analytical methods

All chemical analyses were carried out in the Institute of Geology and Geophysics (IGG), Chinese Academy of Sciences, Beijing. The analytical procedures are described in detail below.

Geochemistry

The rocks were crushed into small pieces and cleaned with deionized water in an ultrasonic vessel for 15 minutes after removal of thin weathered surfaces, amygdales and veins. The dried rock chips were powdered in an agate mill to about 200 mesh for major, trace element and isotopic analyses. Major oxides were determined by X-ray fluorescence spectrometry (XRF) with analytical errors less than 5 %. Loss on ignition (LOI) was determined after igniting sample powders at 1000 °C for 1 hour. Trace elements, including rare earth elements (REEs), were analysed with an ICP-MS Element II. Whole-rock powders (40 mg) were dissolved in screw-top Teflon beakers using a HF + HNO_3 mixture for five days at 200 °C, then dried and digested with HNO_3 at 150 °C twice a day. Finally the dissolved samples were diluted to 50 ml with 1 % HNO_3 before analysis. An internal standard solution containing the single element indium was used to monitor drift in mass response during counting. The precision was generally 2–5 %.

Rb–Sr and Sm–Nd isotopic ratios were measured by a Finnigan MAT262 thermal ionization mass spectrometer (TIMS). The measurements were carried out following the isotope dilution procedures of Zhou *et al.* (2002) and Chen, Hagner & Todt (2000). A static multi-collection mode was used during the measurements. A traditional cation exchange technique was adopted for the chemical separation. Mass fractionation corrections for Sr and Nd isotopic ratios were based on $^{86}Sr/^{88}Sr = 0.1194$ and $^{146}Nd/^{144}Nd = 0.7219$. Repeated measurements of La Jolla Nd standard and NBS987 during the measurement period gave $^{143}Nd/^{144}Nd = 0.511861 \pm 9$ (2σ) and $^{87}Sr/^{86}Sr = 0.710254 \pm 10$ (2σ), respectively. Total procedural blanks for Sr and Nd were $\sim 10^{-9}$ and $\sim 10^{-11}$ g, respectively.

U–Pb zircon geochronology

Zircons crystals were separated by heavy liquid and magnetic techniques from 5–6 kg hornblende gabbro samples, and then hand-picked in alcohol under a binocular microscope and mounted on epoxy resin. The zircon mount was polished with a diamond compound to reveal the zircon midpoints. To identify the internal features of the zircons (zoning, structures, alteration, fractures), cathodoluminescent images were obtained with a Cameca electron microprobe. The analytical voltage and current for the CL was 50 kV and 15 nA, respectively. The zircon isotope analyses were undertaken with a Neptune MC-ICP-MS, which has a double focusing multi-collector ICP-MS and has the capability for high mass resolution measurements in multiple collector modes. The GeoLas 200M laser ablation system (MicroLas, Göttingen, Germany) was used for laser ablation using an ArF excimer 193 nm laser ablation system and a homogenizing, imaging optical system. The isotope measurements were carried out following the procedures of Xu *et al.* (2004), Wu *et al.* (2006) and Yuan *et al.* (2003). Samples were analysed with the ablation of a single 40 μm spot with a laser repetition rate of 10 Hz, and the data were acquired in a peak-jumping-pulse counting mode with one-point measured per peak. Zircon 91500 was used as the external calibration standard, and we measured this zircon after finishing analyses of every four or five spots in order to keep the instrument in comparable conditions when measuring the standards. $^{207}Pb/^{206}Pb$ and $^{206}Pb/^{238}U$ ratios were calculated using GLITTER 4.0, which was then corrected using Harvard zircon 91500 as an external standard. The concordia ages and diagrams were calculated using Isoplot (ver. 2.0).